Eidgenössische Technische Hochschule Zürich
Swiss Federal Institute of Technology Zurich

Method Refinement and Characterization of Bulk Acoustic Wave Resonators for Brillouin Optomechanical Frequency Conversion

Master's Thesis

Michael von Arb
mvarb@student.ethz.ch

Laboratory for Solid State Physics
Departement of Physics, D-PHYS
ETH Zürich

Supervisors:
Prof. Dr. Yiwen Chu
Maxwell Drimmer

January 20, 2022

Abstract

Bulk acoustic wave (BAW) resonators show great potential as an intermediary for microwave to optical transduction as they provide access to long lived and high-frequency phonon modes both optomechanically and piezoelectrically. In order to choose an optimal material and resonator shape we must know the phonon lifetime, the photoelastic interaction strength and the Brillouin frequency. In this work we present alignment and thermalization improvements and subsequent results of our Brillouin spectroscopy setup that allows us to measure phonon modes in BAW resonators by means of stimulated Brillouin scattering (SBS). Results in plano-convex quartz crystals show phonon mode lifetimes up to 500 μs at 4 Kelvin. Furthermore we were able to measure SBS in a flat-flat calcium fluoride (CaF_2) crystal at cryogenic and room temperature. The improved setup can be used to characterize future samples.

Contents

Chapter 1

Introduction

Research in quantum information processing has risen to an important and popular topic in physics. Superconducting qubits operating at sub-Kelvin temperatures and at microwave frequencies($\sim$ 10 GHz) provide a promising platform for building quantum computers [1]. As for classical information, there will be the demand for sharing and therefore linking nodes together into a quantum network [2]. A big challenge is to provide long distance links that are able to maintain the quantum character of the information [2, 3]. While a short distance cryogenic link has already been achieved [4], most likely a feasible long distance connection at room temperature is only possible by means sending photons through optical fibers. Therefore the challenge is to convert quantum states from the microwave to the optical domain ($\sim$ 200 THz), where low loss transmission at room temperature is possible [5]. The converted photons can be transmitted over long distances and reconverted to the microwave domain at the receiving dilution refrigerator. The crucial part within this process is the microwave-to-optical transducer in both directions. Another approach to this challenge involves entanglement swapping, where two photons from two fridges are interfered to create entanglement between the microwave circuits, without directly transporting the information from one fridge to the other [6].

The goal is to find a way to engineer such a microwave-to-optical transducer and implement it with maximal conversion efficiency and minimal added noise. One approach to achieve to transduction is direct electro-optical coupling. This has the advantage of a large conversion bandwidth but struggles with low conversion efficiency [7, 8]. Another approach we focus on, is to use an intermediate system that strongly couples to both microwave and optical frequencies. A good candidate for this are mechanical resonators coupling to a wide range of systems such as superconducting circuits [9], NV centers [10] and optical light [11]. Therefore the transduction is a three system process where the superconducting qubit interacts electromechanically with the resonator, which in turn interacts optomechanically with the light.

The field describing the interaction between the mechanical resonator and the modes of an optical cavity is called *cavity optomechanics* [11]. Over the last 15 years, researchers have been able to optically control long-lived phonons. The quantum applications of this field are in microwave-to-optical transduction [12, 13] and long-lived storage of quantum states [14]. During this time, important results in quantum measurement and precision metrology such as ground state cooling [15], entanglement of mechanical resonators [6] and force and displacement measurement below the standard quantum limit [16] have been achieved. The large variety of mechanical resonators open for design engineering

resulted in several different implementations like a whispering-gallery mode cavity with a mechanical microdisk [17], a photonic crystal cavity with a nanomechanical string [18] or a Fabry-Pérot cavity with a membrane in the middle [12]. In a similar setup to the latter was used to measure the highest transduction efficiency to date, 47% [19].

One promising optomechanical interaction involves BAW resonators [11, 20]. BAWs can be generated in bulk crystals, whose surfaces can act like mirrors for the acoustic waves, creating long-lived and stable phonon modes [21]. Until 2018, phonons in BAW resonators have only been generated piezoelectrically, but it has been proven that it can also be done optomechanically. This less invasive optical approach has achieved a promising high frequency quality factor product (fQ), which is a measure of phonon coherence [20]. BAWs offer the advantage of being less susceptible to surface interactions, making them promising candidates for microwave to optical transduction in the strong coupling regime. This is the reason why we use them in our laboratory as an intermediate between superconducting qubits and light. However, the question of which material is optimal for this device has not been answered yet. The largely unexplored parameter space of appropriate material and surface shape has to be investigated to find the sample that minimizes phonon and qubit dissipation, has a high enough photoelastic interaction, and suitable Brillouin frequencies.

Therefore in this thesis we present the setup, improvements, and results of a phonon mode spectroscopy method and measure stimulated Brillouin scattering in BAW resonators. We have characterized plano-convex quartz and flat-flat calcium fluoride crystals at cryogenic and room temperatures. Characterization of crystal samples at cryogenic temperatures will be of particular use for building an optomechanical cavity system for BAW resonator intermediated microwave-to-optical transduction.

This introduction is followed by theoretical approach to Brillouin scattering and a summary of previous experiments in this field (section 2). In chapter 3 we describe our measurement setup and method followed by chapter 4, which presents measurement data and characterisation results. Afterwards chapter 5 is about the refinements of the setup (crystal mount, alignment and beam waist), which I improved in the course of the master thesis. Finally, the conclusion and outlook is presented in chapter 6.

Chapter 2

Background

In this section we explain the theory behind Stimulated Brillouin Scattering, how to approximate the Brillouin frequency of a material, and discuss the features of a typical SBS measurement. Furthermore we give a overview of related experiments that have been done already.

2.1. Stimulated Brillouin Scattering

Stimulated Brillouin Scattering (SBS) is a non-linear scattering process that was experimentally observed for the first time by Chiao and Townes in 1964 [22]. SBS is a three wave mixing process of two optical waves and one acoustic wave. The interference pattern between the two optical waves change the refractive index of the medium. The reason for this is electrostriction, the tendency of material to compress where there is an electric field. The resulting density differences lead to an altered refractive index. The inelastic scattering at these periodic density fluctuations lead to frequency shift of light and creation of sound waves, as depicted in figure 2.1a.

Due to energy conservation, the frequency difference between the optical beams must match the frequency of the sound wave $\Omega_S = \omega_p - \omega_S$, where initial (pump) photon with frequency ω_p scatters into a Stokes photon with frequency ω_S and a phonon. Note that in this work we follow this Stokes process. There is also the anti-Stokes process, which is again a three wave mixing process but goes the other way (one phonon and one photon create a photon) with frequency relation $\Omega_{AS} = \omega_{AS} - \omega_p$. The scattering can be stimulated by the interference of the initial (pump) and scattered (Stokes/probe) light that contains a frequency component at the differences of frequency $\omega_p - \omega_S$, which is equal to the frequency Ω_S of the sound wave. The density fluctuation response of the material to this interference can act as a source that increases the amplitude of the sound wave. Thus both the beating of the pump wave with the sound wave reinforces the Stokes wave, whereas the beating of the pump with the Stokes wave reinforces the sound wave creating a positive feedback that leads to an exponential growth of the Stokes wave.

For the experiments in this thesis we will use a configuration called SBS amplifier, where both the pump and the Stokes field are applied externally. A schematic picture of the three wave vectors in the crystal is shown in figure 2.1b. The pump beam moving in forward direction in blue with wave vector k_p and the counter propagating Stokes (red) beam with wave vector k_S creating sound waves moving in forward direction with wave vector q_S (green). Resonant coupling occurs only if the frequency of the Stokes light ω_S

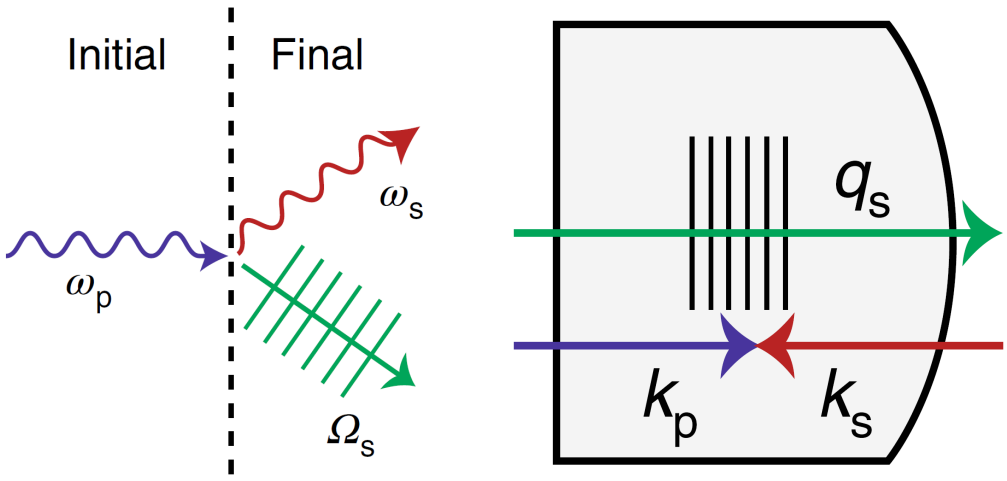

a. frequencies b. wave vectors

Figure 2.1.: Principle of SBS: (a) pump beam coming the left side with frequency ω_p and wave vector k_p (blue) scattering in to counterpropagating Stokes beam (ω_S, k_S, red) and the acoustic wave (Ω_S, q_S, green). (b) Momentum conservation constraint $q_S = k_p + k_S$ is shown in the length of the wave vectors. (Figures from [20])

is approximatively related to the scattered pump light as [23]:

$$\omega_S = \omega_p - \Omega_B. \tag{2.1}$$

Here Ω_B is the Brillouin frequency. It is related to the acoustic wave vector by the phonon dispersion relation $\Omega_B = |\vec{q}_B| v_a$, where v_a is the acoustic velocity of the material. The assumption of this sound wave being driven by the beating of the pump and the Stokes light gives the relation between the wave vectors

$$\vec{q}_B = \vec{k}_p - \vec{k}_S. \tag{2.2}$$

As a result of that the best beam configuration is counterpropagating. The optical wave vectors in this momentum conservation relation are related to the corresponding frequencies via $|\vec{k}_p| = \omega_p / v_0$, respectively $|\vec{k}_S| = \omega_S / v_0$, where v_0 is the phase velocity of light in the medium. Inserting the dispersion relations into equation (2.2) and knowing that the pump and Stokes waves are counter propagating leads to the expression for the Brillouin frequency

$$\Omega_B = \frac{v_a}{v_0}(\omega_p + \omega_S).$$

Together with equation (2.1) the Brillouin frequency in terms of the pump frequency ω_p can be obtained:

$$\Omega_B = \frac{\omega_p v_a / v_0}{1 + v_a/v_0} \approx \frac{2 v_a \omega_p}{v_0} \tag{2.3}$$

The approximation uses the fact that the speed of sound is much smaller than the speed of light in the medium ($v_a \ll v_0$) [23].

In practice the externally imposed probe wave has a known frequency ω_S. The frequency detuning between the the pump and the probe frequency $\Omega = \omega_p - \omega_S$, which is the frequency of the driven acoustic wave, is in general different from the Brillouin frequency Ω_B from equation (2.3). Thus the acoustic wave will only be excited efficiently if ω_S is chosen such that the frequency difference $|\Omega - \Omega_B|$ is smaller than the Brillouin linewidth Γ_B [23]. The latter is given by the inverse of the phonon lifetime $\tau_{phonon} = \Gamma_B^{-1}$ in our crystal.

For the experiments presented in this report, we have to consider two different phonon lifetime regimes. The 'Brillouin limit' where phonons decay rapidly and the 'coherent-phonon limit' where phonons are long-lived. The corresponding considerations in this section follow (if nothing else is mentioned) [20] and its supplementary material.

Brillouin limit At room temperature acoustic waves decay rapidly due to intrinsic dissipation [20]. The phonon decay length l_{ph} of order 100 μm is much shorter than the crystal lengths ($L \sim 5$ mm) used in the experiment. Thus the acoustic wave is excited locally due to its interaction with the optical waves and its propagation in space can be neglected. So the expected Brillouin signal can be explained by conventional Brillouin treatments as presented in [20, 23]. The change of Stokes power over the interaction length L is given by

$$\Delta P_s(L) = P_s(0) - P_s(L) \simeq G_{SBS}(\Omega) P_p(0) P_S(L) L, \tag{2.4}$$

assuming an undepleted pump regime ($P_p(z) \approx$ const) with weak signal gain ($\Delta P_s \ll P_s$) [20]. In equation (2.4) $P_p(0)$ ($P_s(L)$) is the power of the pump (probe) beam before the crystal on the pump (probe) side. The Brillouin gain coefficient G_{SBS}, depending on the detuning Ω, that determines the energy transfer from the pump to the probe beam is given by

$$G_{SBS}(\Omega) = \frac{\omega^2 n^7 p_{13}^2}{c^3 v_a \rho \Gamma_B A^{ao}} \frac{(\Gamma_B/2)^2}{(\Omega - \Omega_B)^2 + (\Gamma_B/2)^2}. \tag{2.5}$$

Here we have the refractive index of the material n, the relevant photo-elastic constant p_{13}, the speed of light c, the density ρ and the effective acousto-optic area A^{ao} which is determined by the mode overlap of acoustic and optical fields. The distinction between the beam frequencies ω_p and ω_s was dropped by setting $\omega = \omega_p \simeq \omega_s$.

The second fraction of the gain coefficient (eq. (2.5)) is the reason for the Lorentzian shape of the Brillouin gain spectrum centered at the Brillouin frequency as can be seen in

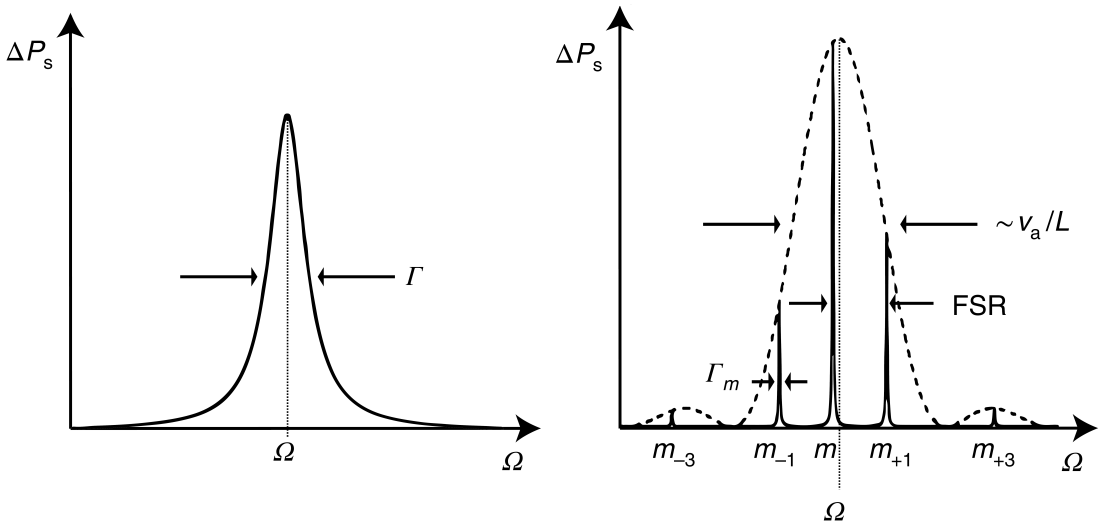

Figure 2.2.: Expected change of probe power over crystal length $\Delta P_s(L)$ depending on the detuning Ω between the pump and the probe beam both for room temperature (a) and cryogenic temperature (4 K) (b). Modified from [20]

figure 2.2. The phonon dissipation rate Γ_B can be determined measuring the linewidth of the gain spectrum. The phonon dissipation rate together with the height of the gain spectrum can be utilized to deduce the strength of the electrostrictive coupling [20].

Coherent-phonon limit At cryogenic temperatures the phonon lifetime is much longer due to reduced acoustic losses at low temperatures. This implies that the coherence length l_{ph} is on the order of meters, which is much longer than the length of the used crystals ($l_{ph} \gg L$). Thus, the propagation of the phonons can no longer be neglected and the mechanical response of phonons is non-local. The acoustic waves reflect off the boundaries of the medium and form standing waves with macroscopic discrete phonon modes with frequencies Ω_m and characteristic wavevectors q_m much like optical modes in a Fabry-Pérot resonator. This changes the character of the energy transfer, such that the dispersion curve becomes discretized instead of being continuous as in the Brillouin limit. The frequency of the mth standing wave acoustic mode in 1D can be approximated as $\Omega_m = 2\pi \times (m v_a)/(2L)$ assuming a linear dispersion. The mode spacing between two neighbouring modes can be described by the acoustic free spectral range (FSR) $\Delta\Omega/2\pi = v_a/2L$.

According to [20] the change of Stokes power over crystal length L in the coherent-phonon limit is

$$\Delta P_s(L) \approx P_p(0) P_s(L) \sum_m \frac{4|g_0^m|^2 L^2}{\hbar \omega_p v_0^2 \Gamma_m} \frac{(\Gamma_m/2)^2}{(\Omega - \Omega_m)^2 + (\Gamma_m/2)^2} \operatorname{sinc}^2\left(\frac{\Delta q L}{2}\right). \tag{2.6}$$

This formula contains the sum over all the phonon modes and can be partitioned into several parts. Most interesting in our case is the Lorentzian part describing the phonon lifetime of each phonon mode. These are the sharp peaks shown in figure 2.2b. Here Γ_m represents the Lorentzian linewidth and accounts for all phonon loss mechanisms such as diffraction losses, intrinsic losses and losses at the surface. The sinc^2 acts like an envelope function and is shown in figure 2.2b with the dashed line, limiting the spectrum to only a discrete set of phonon modes within the phase-matching bandwidth. This is due to the fact that the spacial extent of the standing wave is finite. Here the phase-mismatch between the optical driving and the standing wave phonon mode is described by $\Delta q = q_m - k_p - k_s$, where $q_m = \Omega_m / v_a$.

The change of Stokes power scales with the squared magnitude of g_0^m, the electrostrictive coupling rate of the optical fields to the m^{th} phonon mode. It is calculated from a non-linear susceptibility approach [20] to be approximately

$$g_0^m \approx i \frac{\omega^2 n^3 p_{13}}{2c} \sqrt{\frac{\hbar}{\Omega_m \rho A L}}. \tag{2.7}$$

It depends on an effective acousto-optical area A that is assumed to be constant over the interaction length. Furthermore one can see that the coupling rate and thus the Brillouin signal depends on the relevant photoelastic coefficient p_{13}, which depends on the material and geometry of the sample [20].

2.2. Previous experiments

One goal of our hybrid quantum systems group is to transduce quantum information between microwave circuits, sound and light. A lot of research in the acousto-optic field was done by experts in close relation with our group. Tools for analytical and numerical understanding of acoustic beam propagation in anisotropic solids [20, 24] and fabrication techniques for tailored plano-convex acoustic cavities have already been developed [24]. Optomechanical coupling to long-lived, high-frequency phonon modes within macroscopic bulk acoustic resonators (BAW) at cryogenic temperatures has been demonstrated for different materials (such as quartz, TeO_2 and silicon) [20, 24]. For a flat-flat quartz crystal placed within an optical cavity access to high-frequency phonons has been shown. In the optical cavity, two modes spaced by the Brillouin frequency are used instead of free space beams. The enhanced photon number in cavities dramatically increases the optomechanical coupling [25]. Actually, in such a setup the strong coupling regime between infrared light and bulk acoustic phonons has been reached [26]. In the strong coupling regime the optomechanical coupling rate is higher than both the optical and mechanical losses, which is an even stricter requirement than just the basis requirement of large cooperativity for efficient phonon control using light.

In order to perform and improve acousto-optic transduction, we built a phonon mode spectroscopy device in our laboratory. This will allow us to investigate and characterize different materials and shapes in order to find candidates for optimizing a transducer. My

supervisor Maxwell Drimmer started building up an in-house stimulated Brillouin spectrometry apperature based on the experimental setup and the insight from *Renninger et al., Bulk crystalline optomechanics (2018)* [20]. After the successful construction of the apparatus, he managed to measure a cryogenic SBS signal in flat-flat quartz crystals. A first measurement with plano-convex quartz crystal was also performed. Nevertheless, the results before this thesis showed some unsolved issues as broad peak linewidth, no flat background, obscure peak pattern and broad phase-matching bandwidth. In this work we improve the setup to solve most of these challenges.

Chapter 3

Experimental Setup

The presented stimulated Brillouin scattering amplifier setup in this section allows us to perform phonon mode spectroscopy on our crystalline samples.

3.1. Measurement concept

As the Brillouin signal is quite weak (about one per 10^5 photons is converted), we chose a measurement technique that increases the signal-to-noise ratio. Lock-in detection is used to sensitively measure a signal of known frequency buried in a sea of broadband noise. This technique provides a zero-background measurement of a frequency component from DC to 50 MHz (limited by the bandwidth of the instrument). But our optical signals have frequencies of a couple of hundred terahertz. To solve this issue, we use a homodyne detection scheme: We modulate our input pump light such that we can measure the beat note imprinted on the probe beam by converted photons. The optical beat note can be translated into an electrical signal and is in the detection range of the lock-in amplifier.

The lock-in amplifier is used to measure the amplitude and phase of a signal of known frequency in a noisy environment. It takes two RF signals as inputs. The following two example signals are here to illustrate the process, but the scheme also works with other input signals. The first signal is the one to measure $V_s = \frac{1}{2}A_s(e^{i\omega_s t} + e^{-i\omega_s t})$ and the second one is the reference signal $V_r = 2A_r e^{-i\omega_r t}$ with the ω_r frequency of interest. First the two signals are mixed $V_s \cdot V_r = A_s A_r(e^{i(\omega_s-\omega_r)t} + e^{i(\omega_s+\omega_r)t})$. After that a low-pass filter cuts all unwanted higher frequencies, thus only the first term survives. The remaining low frequencies, ideally a DC signal and at least smaller than the cut-off frequency of the low-pass filter, can be measured. This signal is proportional to the amplitudes of the signal at the reference frequency $A_s(\omega_r)$ times the amplitude of the reference A_r. By means of trigonometric operations the amplitude and the phase of the signal can be obtained [27].

This means for our experiment that the pump frequency needs to be modulated with a reference frequency Δ such that the beat note of the signal can be measured with lock-in detection at the modulation frequency Δ.

Intensity modulating the pump signal affects the Stokes power. Therefore it is not only light at pump frequency ω_p but also light at the two additional sideband frequencies $\omega_{p\pm1} = \omega_p \pm \Delta$ that interacts with light at probe frequency $\omega_s = \omega_p - \Omega$. This implies that pump light from the sidebands scatters phonons created at the detuning frequency Ω creating sidebands of probe light with frequency $\omega_{s\pm1} \approx \omega_s \pm \Delta$. In fact the lock-in

detection measures the magnitude of the beat note of the probe with its sidebands.

The change in the probe sideband power depends on the frequency and amplitude of the intensity modulation of the input pump beam Δ. As the signal in the Brillouin limit is quite weak the power measured at the lock-in detector is highest when the intensity modulation is smaller than the Brillouin linewidth ($\Delta \ll \Gamma_B$). In this limit the lock-in power can be expressed as

$$P_s(lock{-}in) = 4G_{SBS}LP_{s0}\sqrt{P_{p0}P_{p-1}},$$

depending on the probe power P_{s0} on the probe side and both the pump powers of the carrier P_{p0} and the sideband P_{p-1} on the pump side of the crystal.

The SBS signal in the coherent limit is more complex, the signal structure is easier to resolve when the intensity modulation is much bigger than the phase-matching bandwidth $\Delta \gg \Delta q$. Therefore there are no overlapping contributions from the three pump tones. In this limit the lock-in power at cryogenic temperatures is given by

$$P_s(lock{-}in) = \frac{8}{\hbar\omega v_0^2 \Gamma_m}|g_0^m|^2 L^2 \sqrt{P_p(0)P_{p-1}(0)}P_s(L),$$

where $z = 0$ ($z = L$) is at the pump (probe) surface of the crystal sample [20].

We have found that it is advantageous to measure at intensity modulations $\Delta = 487$ kHz at room temperature and higher modulations like $\Delta = 20$ MHz at cryogenic temperatures. However modulation at higher frequencies comes at the cost of less efficient modulation and therefore lower modulation depth.

3.2. Measurement diagram

In order to measure a Brillouin signal, we have set up our experiment that consists of a fiber-optical and a free space part. First let's look at the fiber-optical part where the initial beams are generated and the signal is measured, a schema of which is shown in figure 3.1.

Both beams (pump and probe) originate from a narrow (10 Hz) linewidth Pure Photonics laser with a wavelength centered around 1550 nm. Directly after this, the light is split into the pump (blue) and the probe arm (red), using a 90:10 beam splitter. The probe light is then phase modulated by the detuning frequency Ω with a phase modulator (PM). A narrow bandpass filter ((BPF), 4 GHZ bandpass bandwidth, 40 dB suppression [28]) with its transmission range at the lower first sideband filters out all the unwanted contributions from the phase modulation including the carrier. The resulting probe beam is amplified (by the Amonics EDFA), polarization aligned to the pump beam and guided into the free space part described below. 1 % of the probe light is sent through a variable optical attenuator (VOA) and connected to the input of a balanced detector as a reference.

In order to perform a lock-in measurement as described in the section above the pump beam is intensity modulated (IM) directly after the split of the two laser arms. After

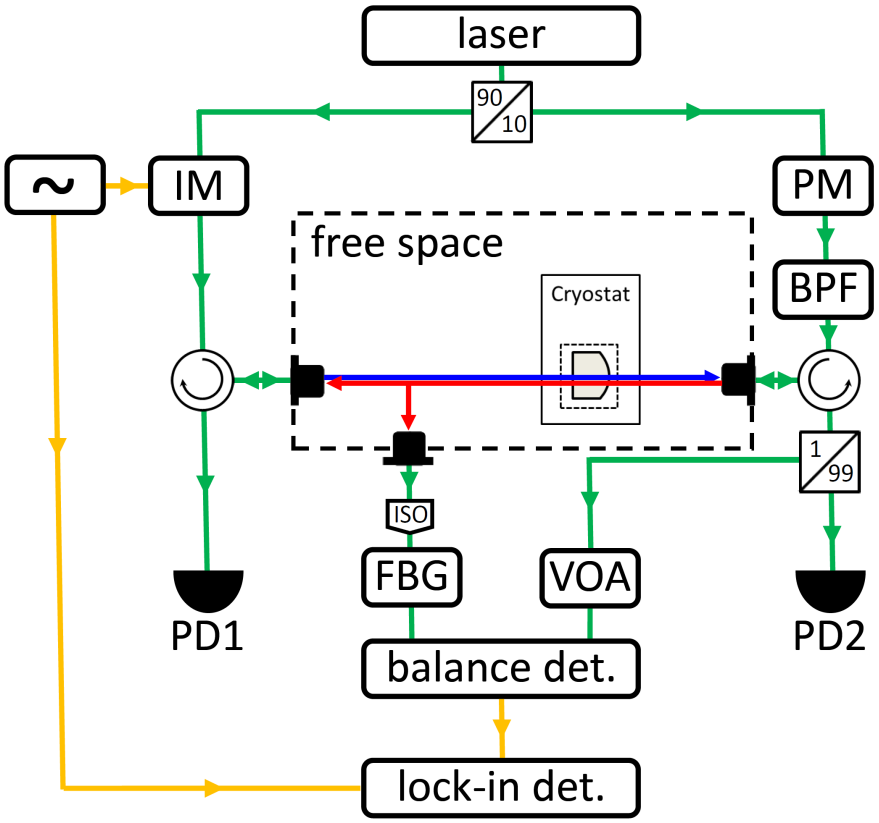

Figure 3.1.: Fiber setup with the pump path on the left side and the probe path on the right side. Color code: Electrical signals (yellow), light in fibers (green), light in free space (blue (pump) and red (probe))

amplification with the TV Direct EDFA the pump beam is led to free space part of the experiment.

Circulators are set in before each of the collimators that send light into free space. Additionally they allow the surveillance of the light coupling in reverse direction via photodetectors (PD). In addition, the circulators prevent light from entering into the input arms in the wrong direction creating interference.

The pump and probe beams enter the free space part from opposite directions through collimators which in our case are pigtailed GRIN (graded-index) fiber optic couplers. A more detailed schema of the free space part is shown in figure 3.2. Each beam that enters free space is reflected at a mirror first. These two additional degrees of freedom (x- and y-tilt) enable control over the position and angle of the beams. Then they are focused by a lens onto the sample crystal in the cryostat. Within the cryostat we are able to cool the crystal down to a temperature $T = 4$ K. It has two transparent windows on each side such that the beams can enter. To spatially separate the Brillouin signal path from the incoming one, a 92:8 beam splitter is placed between the mirror and the

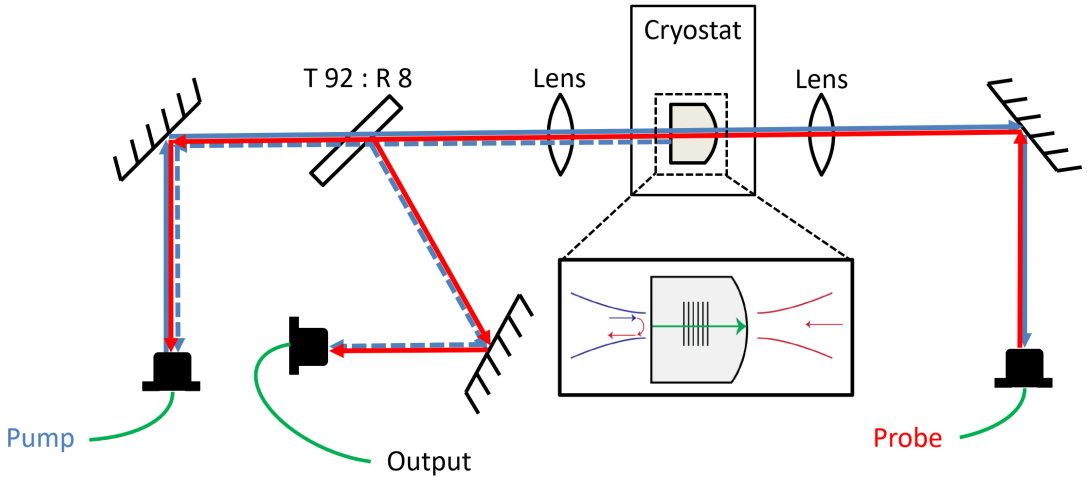

Figure 3.2.: Schema of the free space part of the setup. The direct beam paths of the pump (blue) and the probe (red) are drawn in solid lines whereas relevant reflections from the flat surface of the crystal are depicted in dashed lines. Inset from [20]

lens on the pump side. The reflection of the beam splitter is collimated at the output GRIN coupler after being reflected by a mirror. From this point on the signal is again processed in fiber optics.

The goal of the measurement is to measure the Brillouin signal on top of the probe. Additionally, the out-coupled signal contains the reflected pump beam. To get rid of the latter the out-coupled signal is filtered out with two serial fiber Bragg gratings (FBG) each with 30 dBm suppression [29]. The isolation (ISO) is done using circulators before and between the FBGs, such that reflections can't go back into free space. The remaining Brillouin Signal is input to the balanced detector (Thorlabs PDB415C) where an output voltage (RF OUTPUT) is generated proportional to the difference between the Brillouin signal on top of the probe and the probe reference. Hereby we can suppress common fluctuations of the probe and reach higher signal-to-noise ratios and higher sensitivity. The balanced detector measures the input powers as well, allowing us to match power of the output light after the FBGs and the reference in order to measure the desired frequency with lower noise [30, 31].

After the balanced electrical output signal is sent to the lock-in amplifier, it is mixed with the modulation signal from the signal generator. As described in the previous section, in doing so we can measure the power of the Brillouin signal in the probe sideband, which allows us to determine the Brillouin gain and coupling rate for room temperature and cryogenic measurements. A photo of the free space part of experimental setup can be seen in figure 3.3.

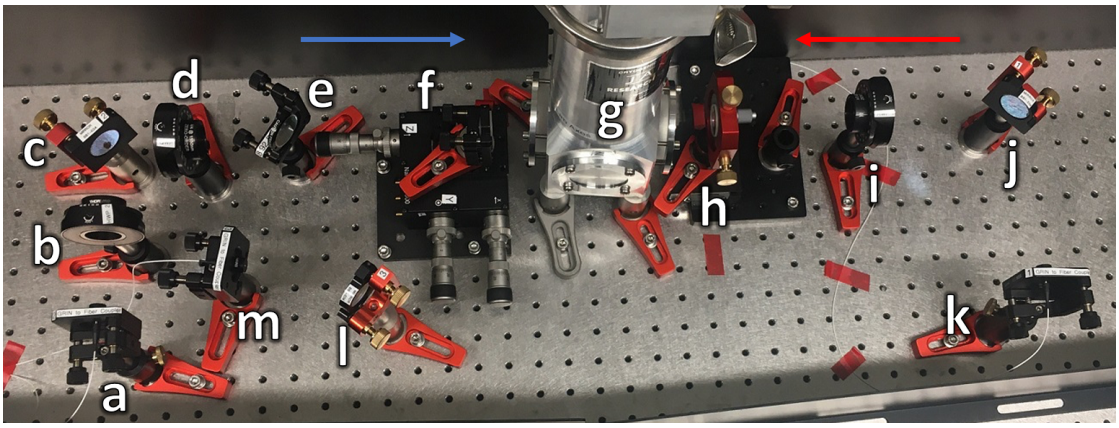

Figure 3.3.: Photo of the free space measurement setup with pump beam (blue) coming from the left side and probe beam (red) coming from the right side. Components: Free space collimators: (a),(k),(m); Mirrors: (c),(j), (l); Lens on 3-axis translation stage (f); Lens on z-direction translation stage (h); Cryostat with crystal sample inside (g); Beam spliter: (e); Wave plates: (b), (d), (i)

Chapter 4

Results

The experiments were performed for two plano-convex quartz crystals ($L = 5$ mm, $r_c = 30$ mm and $L = 5$ mm, $r_c = 10$ mm) and two flat-flat crystal calcium fluorite and magnesium fluoride (MgF_2)(both with $L = 1$ mm). Brillouin signals were measured at room and cryogenic temperatures. To determine the Brillouin response of each sample, we swept the detuning frequency between the pump and the probe laser frequency while simultaneously measuring the lock-in signal. In this section, the best results (which were obtained after several improvements of the setup) are presented. The aforementioned improvements will be explained in detail in Chapter 5.

4.1. Quartz

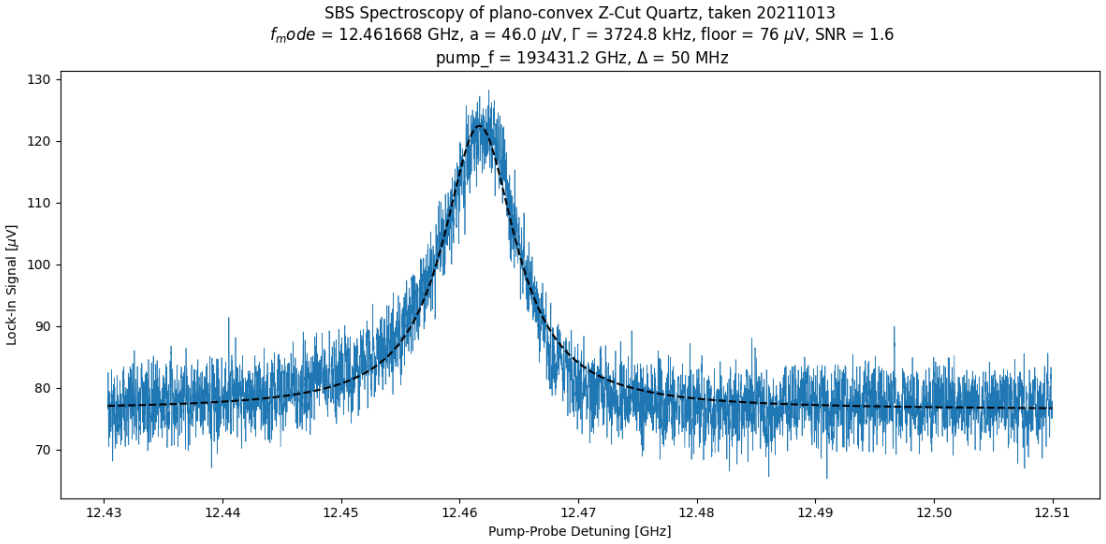

Figure 4.1.: Room temperature lock-in signal with quartz plano-convex crystal ($r_c = 30$ mm)

The first experiment was performed at room temperature using a plano-convex quartz crystal with length $L = 5$ mm and radius of curvature (ROC) $r_c = 30$ mm. The intensity modulation Δ was fixed at 487 kHz (such that $\Delta \ll$ phase matching bandwidth). The pump frequency was set at 193431.2 GHz. Figure 4.1 shows the lock-in signal of the

pump-probe detuning sweep from 12.43 GHz to 12.51 GHz. The data is averaged over 5 sweeps and shows a clear peak. The Lorentzian fit indicates the peak at 12.4617 GHz. It shows also a peak linewidth of 3.7 MHz, a signal to noise ratio (SNR) of 1.6 and a noise floor of 76 μV. Identical measurements with a 10 mm ROC crystal lead to similar results.

As the measurement is performed in the Brillouin limit the phonons in the crystal are expected to decay rapidly leading to a Lorentzian shaped Brillouin scattering peak. This can be seen well in our results. The Lorentzian fit displayed as a dashed line matches well with the lock-in signal. The SNR is good enough to see a clear peak even for a low number of averaged sweeps. The measured linewidth demonstrates a phonon lifetime (coherence length) of $\tau_{ph} = \Gamma_B^{-1} \sim 2.7 \cdot 10^{-7}$ s ($l_{ph} = v_a \Gamma_B^{-1} \sim 1.7$ mm) which is consistent with existing data [20]. The theoretically predicted Brillouin frequency for quartz $\Omega_{B,quartz}$ obtained by equation (2.3) is 12.5 GHz when using the quartz speed of sound $v_a = 6319$ m/s and refractive index $n = 1.53$. Our signal shows a Brillouin frequency of 12.46 GHz which is close to the theoretical prediction and a satisfying result. This gives a good indication that the measurement at cryogenic temperature will be successful.

To investigate the performance in the coherent phonon limit, the same experiment was performed at 4.2 Kelvin. This was done with two different crystals, one with radius of curvature $r_c = 30$ mm as before (Fig. 4.2) and the second with radius of curvature $r_c = 10$ mm (Fig. 4.3). Figure 4.2a shows the lock-in signal of the pump-probe detuning sweep from 12.65 GHz to 12.67 GHz at an intensity modulation $\Delta = 20$ MHz. The shape of the signal at cryogenic temperatures looks different than at room temperature. The lock-in signal here contains many sharp and equally spread peaks within a bandwidth of about 11 MHz. Also the peak height is much higher. The envelope of the signal in figure 4.2a has three maxima with increasing heights.

To investigate individual phonon modes, we zoom in close to the highest peak. Figure 4.2b shows the spectrum over a range of 1 MHz. It looks like the peak pattern of three peaks is repeated. Here, we will call these patterns families. The first and highest peaks of a family can be fitted by Lorentzians. The fits have linewidths of $\Gamma_1 = 2.1$ kHz (at 12.660076 GHz) resp. $\Gamma_2 = 2.2$ kHz (at 12.660705 GHz) and SNRs of 13.7 resp. 9.4. The frequency distance between this peaks is thus 629 kHz. The frequency differences between peaks within the family are 107 kHz between the first and second peak at 12.660183 GHz and 213 kHz between the first and third peak at 12.660289 GHz.

This measurement at 4 K agrees with the predictions for the coherent limit. The highest sharp peak matches very well the Lorentzian fit (dashed line). Their narrow linewidth correspond to coherence length $l_{ph} \sim 3$ m, what confirms that we are in the coherent limit ($l_{ph} \gg L$). Thus only the phonon modes supported by the acoustic cavity in the crystal survive and couple to the optical modes leading to the present sharp peaks.

The supported phonon modes within BAW resonators of arbitrary material and surface shapes can be simulated by means of a beam propagation code. It finds the modes by propagating the acoustic field inside the crystal back and forth, where the initial

a.

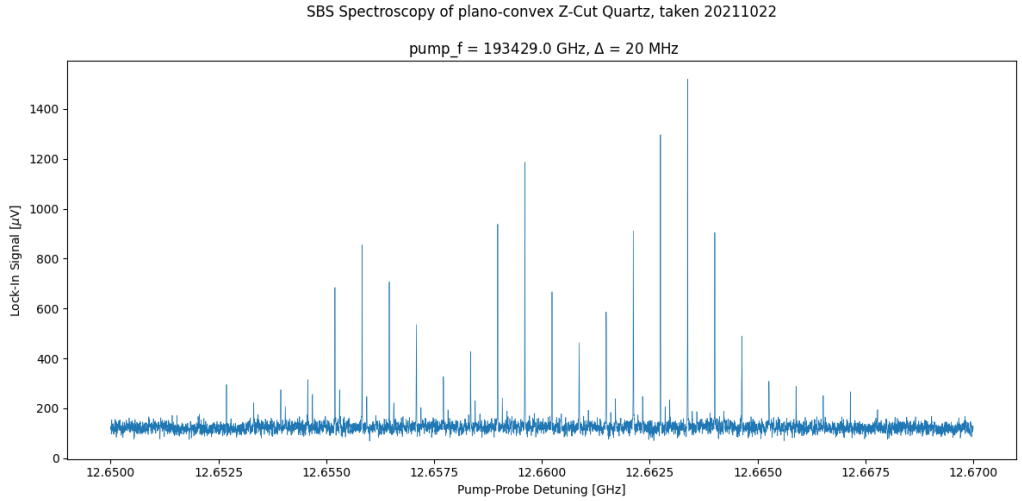

b.

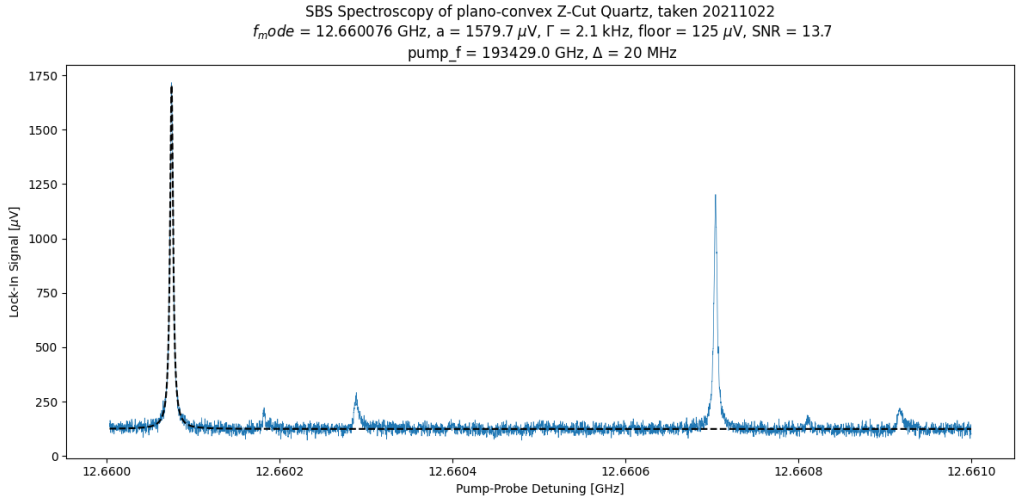

Figure 4.2.: Lock-in signal for plano-convex quartz with $r_c = 30$ mm at $T = 4$ K using an intensity modulation frequency $\Delta = 20$ MHz

field can be chosen [33]. It even allows one to simulate the higher order phonon modes supported by the crystal [20]. The predicted FSR of the acoustic cavity from the beam propagation code is $\Delta_{FSR} = 632$ kHz. This matches very well with frequency difference between the highest peaks of the families. Moreover the beam propagation simulations provide validation for all the different peaks within the families. Assuming we have good alignment of the optical beams to the center of the quartz crystal (see section 5.2) simulations predict the light to couple most to the fundamental (00 Laguerre-Gaussian (LG)) phonon mode. The intensity distribution of sixteen LG modes is shown in figure 4.4. Therefore, as $\Delta P_s(L) \propto |g_0^m|^2$, the highest peak originates from the fundamental phonon mode. The beam propagation simulations predict further higher order acoustic modes for our plano-convex quartz sample with $r_c = 30$ mm), namely the asymmetric 01 LG

a.

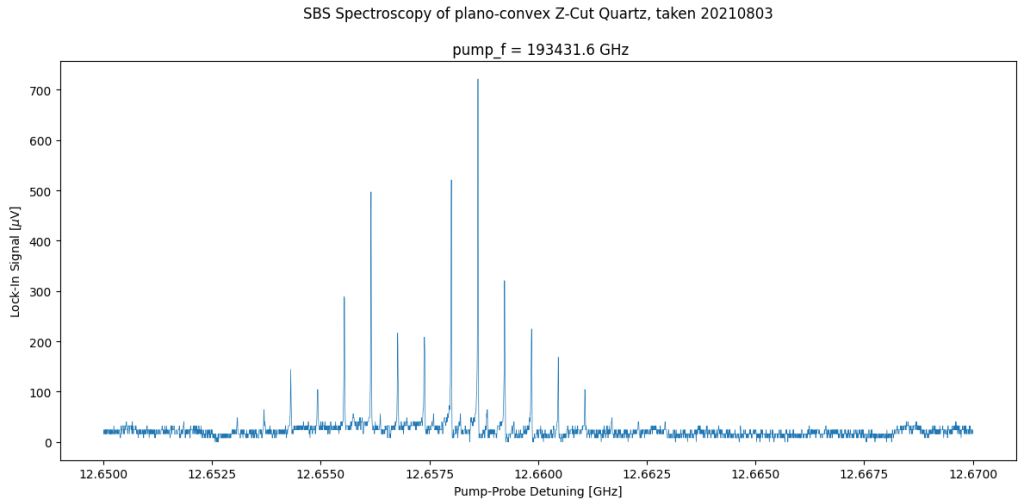

b.

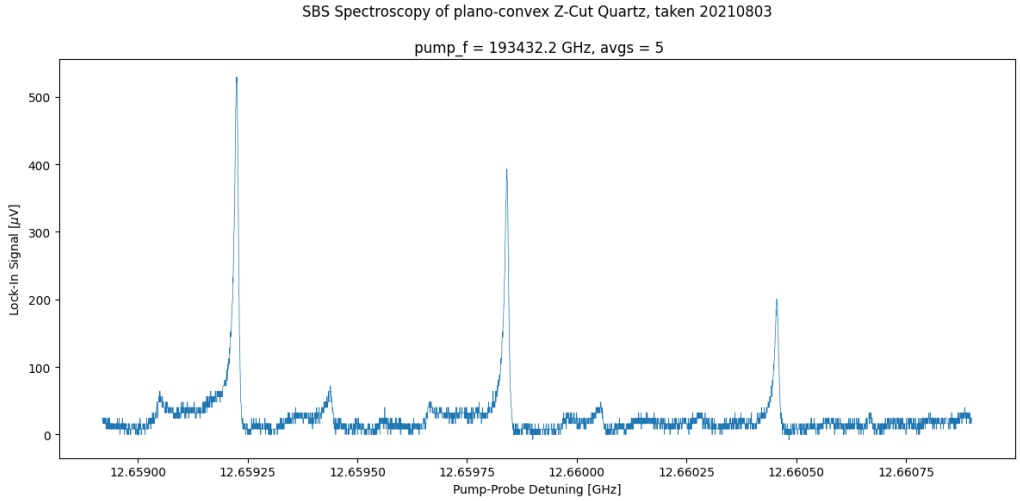

Figure 4.3.: Lock-in signal for plano-convex quartz with $r_c = 10$ mm at $T = 4$ K using an intensity modulation frequency $\Delta = 50$ MHz

and the symmetric 10 LG mode with frequency differences 106 kHz, respectively 213 kHz, to the fundamental mode [33]. These simulations are in excellent agreement with the spectrum we see in figure 4.2b. Having central alignment explains the coupling to the symmetrical modes being higher than the coupling to the asymmetric mode. Therefore it explains as well the different signal heights.

At first view the measured data with the second quartz crystal of length $L = 5$ mm and ROC $r_c = 10$ mm shows similar properties. Nevertheless taking a closer look, differences can be found. The the measurement data in figure 4.3a was taken over a frequency range of 20 MHz. Compared with the 30 mm ROC crystal the phase-matching bandwidth is with 5 MHz (about a factor of two) smaller and the highest peak is at a slightly different

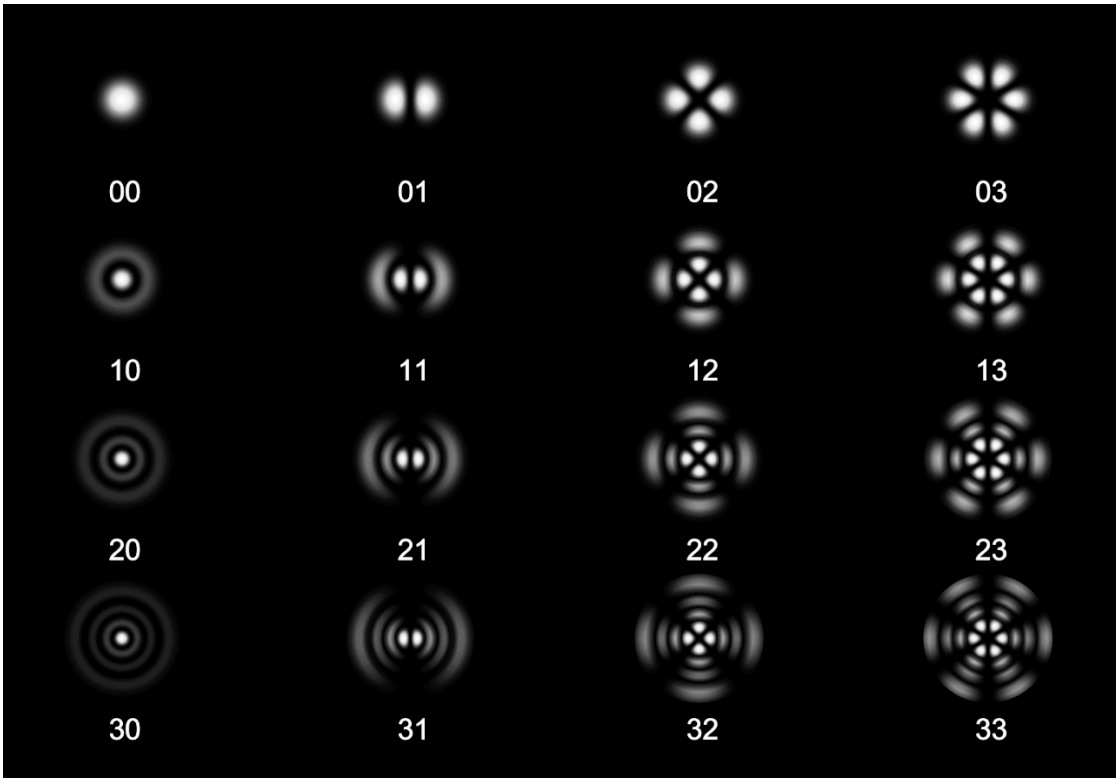

Figure 4.4.: Intensity distribution of LG modes [32]

frequency detuning. A zoom into the range from 12.6589 GHz to 12.6609 GHz (fig. 4.3b) shows the mode families again. Here the frequency difference between two highest peak of two families is 616 kHz. The peaks within a family are spread differently with frequency differences between the first and second (third) peak of the first family showed is 212 kHz (443 kHz).

With the help of the beam propagation code it is possible to validate the spectrum again. The simulations for the plano-convex quartz crystal with ROC $r_c = 10$ mm gives the same FSR $\Delta_{FSR} = 632$ kHz as for the 30 mm ROC crystal. This is reasonable as the length $L = 5$ mm and the speed of sound $v_a = 6319$ m/s is the same for both crystals. But the measured FSR of 616 kHz is close to the theoretical prediction. The simulated higher order phonon modes have a frequency difference of 214 kHz and 427 kHz between the fundamental 00 LG and the asymmetric 01 LG, respectively the symmetric 10 LG mode, and match the results as well. Possible reasons for the small discrepancies can be a small difference in the crystal length L or in the speed of sound v_a of the sample.

Our most significant unresolved issue is the different phase-matching bandwidth and envelope profile. Neither measurement matches the theoretical predictions of a sinc^2-envelope. The suggested bandwidth is of the order of twice the FSR which in this case is about 1.2 MHz [20]. A possible reason for this can be misalignment of the beams [34]. Even though the same aligning procedure was used for the two measurements, it can be

that the alignments are different and even a bit misaligned. The sinc^2-function appears in equation (2.6) because of geometric considerations, specifically the assumption that the transverse acousto-optic area A is constant over the length of the crystal. When the beams overlap in a more complicated pattern the envelope function should change [34]. Furthermore, we observed that the phase-matching bandwidth almost doubled when changing the sample from $r_c = 10$ mm to $r_c = 30$ mm. Narrowing the phase-matching bandwidth and understanding the envelope profile can be objectives for further investigation, even though it is not fully relevant for finding the Brillouin frequency with the highest coupling rate.

The results with our plano-convex quartz crystal were a success. The measured phonon modes live in the optimal frequency range for microwave to optical transduction with superconducting qubits. Quartz is not a good material to work with near superconducting qubits because of its high dielectric loss. Furthermore a piezoelectric substrate will lead to phonon radiation losses. Therefore, it is interesting to investigate the acousto-optical coupling in non-piezoelectric materials as perspective for having longer lived phonon-modes near a long-lived qubits.

4.2. CaF_2

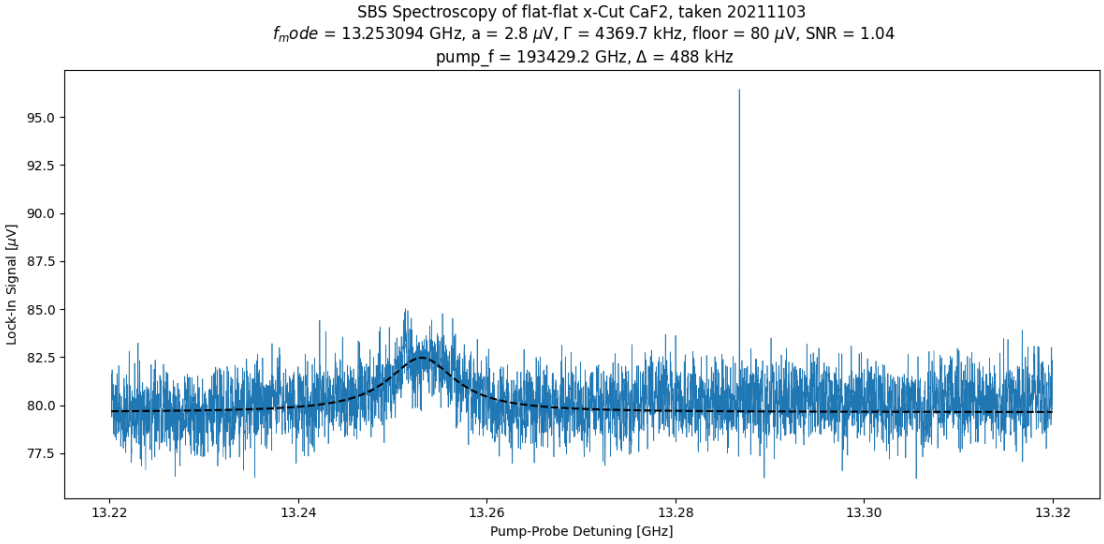

Figure 4.5.: Lock in signal of flat-flat CaF_2 at room temperature

The next investigated sample is a flat-flat calcium fluoride crystal with thickness $L = 1$ mm. The lock-in measurement results at room temperature and intensity modulation $\Delta = 487$ kHz are depicted in figure 4.5. The plot shows the averaged data over 100 probe-pump detuning sweeps from 13.22 GHz to 12.32 GHz. A Lorentzian fit of the

lock-in signal peak with its center at 13.253 GHz has a linewidth of 4.4 MHz and a SNR of 1.04 where the noise level is at 80 μV.

Compared with the room temperature results of quartz the SBS signal of CaF_2 is much weaker. The pump power gain can only be seen after a lot of averaging sweeps, although the relevant photoelastic constant is only slightly lower than the one of quartz [35, 36]. One reason for the lower SNR is certainly the shorter crystal length L as the signal scales with it ($\Delta P_s \propto L$). Another reason is that the relevant photoelastic coefficient is about 25 % lower than the one for quartz. Nevertheless the Lorentzian peak shape matches well with the theoretical predictions for the Brillouin limit (eq. (2.4)).

a.

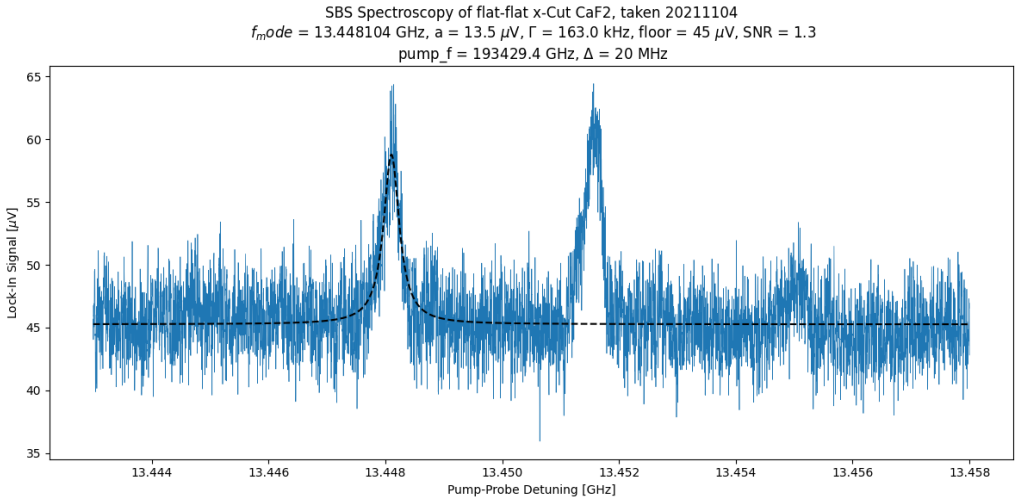

b.

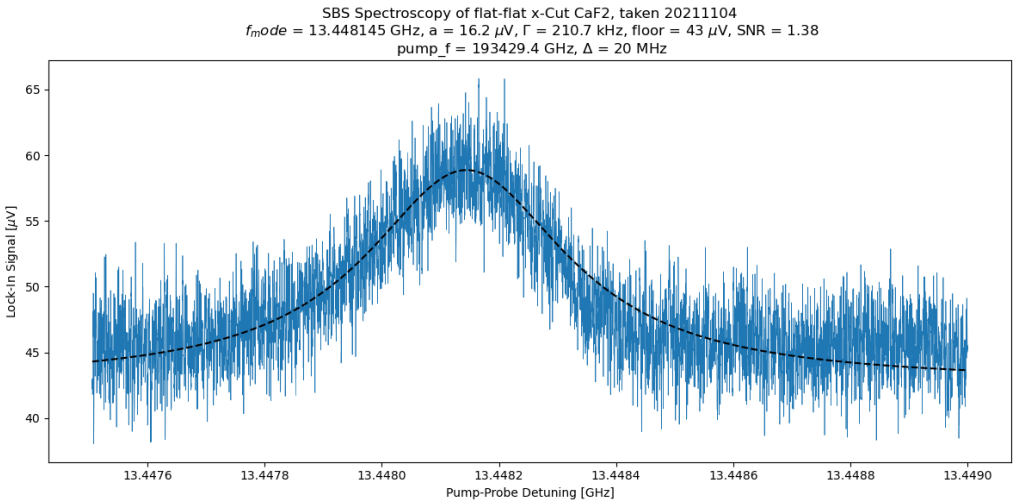

Figure 4.6.: Lock-in signal for flat-flat CaF_2 at $T = 4$ K using an intensity modulation frequency $\Delta = 20$ MHz

Figure 4.6 displays an average of 25 sweeps for the same crystal but at cryogenic temperature $T = 4$ K and intensity modulation $\Delta = 20$ MHz. The full sweep over the

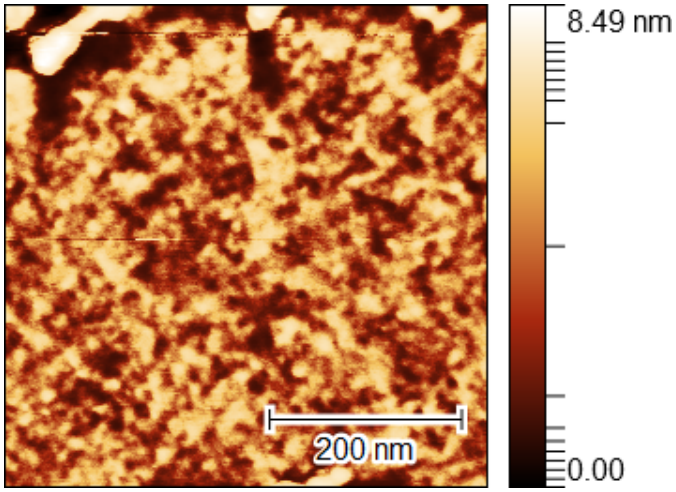

Figure 4.7.: AFM picture of CaF_2 500 nm × 500 nm

signal from 13.443 GHz to 13.458 GHz in figure 4.6a shows three peaks, the third one obviously smaller. The distance between the Lorentzian fit centers of the first and second (resp. second and third) is 3.45 MHz (resp. 3.47 MHz). The Lorentzian fit (dashed black line) of the zoom onto the range around the first peak in figure 4.6b tells us the center frequency $f_{CaF_2,4K} = 13.44810$ GHz, the linewidth $\Gamma = 210$ kHz and SNR of 1.38.

The observed results are in good agreement with the theoretical expectations for the coherent phonon limit. Several peaks originating from even spread acoustic modes are distributed across the phase-matching bandwidth. For a CaF_2 with assumed speed of sound $v_a = 7204$ m/s and crystal length $L = 1$ mm the expected FSR $\Delta_{FSR} = 3.6$ MHz matches the distance between the measured peak center frequencies. Similar to the quartz measurements the signal shape follow well the predicted Lorentzian (depicted with dashed lines). But instead of families with multiple peaks only one broader peak is measured. The crucial difference is the flat-flat surfaces of our sample. Because of the absence of a domed surface the acoustic modes are not well confined in the lateral direction. This leads to more losses and the higher order modes are not distinguishable as the peaks are broadened. We expect the linewidth to account for all phonon loss mechanisms. A simulation of the diffraction limited linewidth for the given sample results in a phonon lifetime of $\tau_{ph} \sim 10$ μs and therefore a expected linewidth of $\Gamma_m = 16$ kHz. Hereby we followed the method of [26, 37]. This is one order of magnitude below of what we measure. The reason for this is possibly an angular misalignment to the normal of the crystal surface. Already a small tilt angle can lead to significant higher loss rates and therefore broader linewidths [26]. The alignment procedure (section 5.2) aims for a pump beam normal to the crystal surface and therefore a minimized tilt angle. Small adjustments of the pump lens tilting angle have not led to significant reduction of the signal linewidth. Nevertheless we have not yet investigated the influence of the tilt angle quantitatively.

Another potential source of scattering that reduces the phonon mode lifetime is the

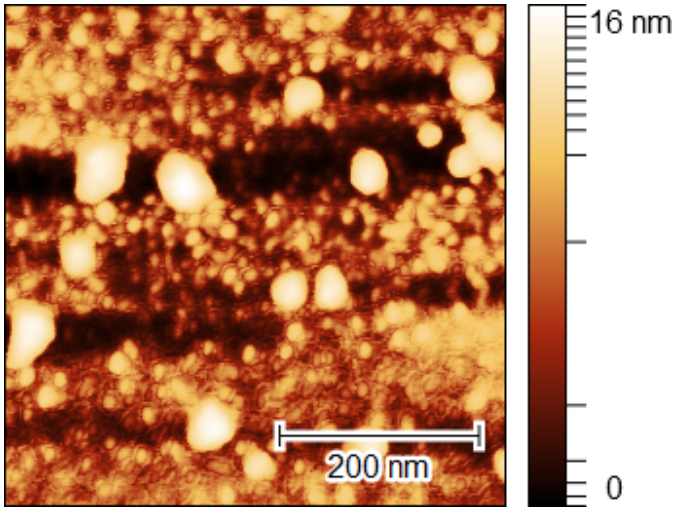

Figure 4.8.: AFM picture of MgF_2 500 nm × 500 nm

surface roughness. To investigate its influence, an atomic force microscope (AFM) scans of the surface of the flat-flat CaF_2 crystal was taken over an area of 500 nm × 500 nm (see figure 4.7). By this means the root mean squared (RMS) roughness of the surface could be determined to be 496 pm. We estimate that scattering losses only play a significant role when the surface roughness is higher than 1 nm RMS, so we don't expect this to be a dominant loss mechanism.

4.3. MgF_2

Magnesium fluoride is another non-piezoelectric material with predicted Brillouin frequency Ω_B between 11 and 15 GHz. Unfortunately we weren't able to measure a SBS spectrum with the flat-flat MgF_2 sample of thickness $L = 1$ mm so far.

As measuring SBS didn't work out we took a AFM picture of the surface of the sample. The picture over an area of 500 nm × 500 nm can be seen in figure 4.8. The RMS roughness of the surface was determined to be 1.59 nm, which is about three times higher than the RMS roughness measured for CaF_2.

The higher surface roughness of the flat-flat MgF_2 crystal is one possible reason that we were not able to measure SBS with this crystal. A higher surface roughness is a source of scattering losses which gives rise to a broader linewidth and lower peaks.

The weaker photoelastic constant $p_{13,MgF_2} = 0.078$ [35] of magnesium fluoride makes it more difficult to resolve a SBS spectrum above the noise floor. Compared to the one of calcium fluoride $p_{13,CaF_2} = 0.202$ [36] and α-quartz $p_{13,quartz} = 0.27$ [35] it is about three, respectively four, times lower. According to equation (2.6) the expected signal scales with the squared of the photoelastic constant p_{13}^2, moreover the refractive indices n, the densities ρ and the acoustic velocities v_a are different.

The quest of the Brillouin signal was complicated by the fact that, to our knowledge,

the Brillouin frequency of MgF_2 has not been measured so far at wavelengths around 1550 nm. And as seen from the results of the CaF_2 crystal the theoretical prediction of the Brillouin frequency from equation (2.3) can be slightly (~ 0.1 GHz) off the actual one. If the Brillouin frequency is only roughly known, the additional difficulties in measuring a SBS spectrum is that to be able to resolve an expected linewidth of a few megahertz at room temperatures the sweep range can not be too high. For achieving sufficient resolution a 25 times averaged scan over 10 MHz takes about 20 minutes. Further the filter restricts the measuring bandwidth (of low background noise). Thus to cover a big range it takes a lot of sweeps. In addition, due to the lower photoelastic constant of MgF_2 its SNR is expected to be lower than for CaF_2. Therefore the signal needs to be averaged more, what requires even more time. Furthermore as long as no signal is measured it's unknown if the noise level is higher than the measured signal. To overcome this possible issue it is planned to use additional FBGs after the out-coupling collimator. We expect those to filter out more backscattered pump light and thus reduce the noise level in our lock-in signal.

Chapter 5

Refinements of the Brillouin spectrometry setup

In order to achieve the results presented in the chapter above, we had to create new sample holders for better thermalization of the sample, adjust measurement settings and domains for better signal resolution and improve the beam alignment procedure and techniques for better acousto-optic overlap and faster alignment. This chapter presents the refinements in more detail and shows how they improved the Brillouin spectrometry results.

5.1. Crystal mount

The refinement with the biggest effect on the signal quality is the new crystal mount that was installed.

The crystal mount is the part of the setup that holds our crystal at the top of the cold finger in the cryostat. Since the cold finger is placed in a vacuum, the crystal mount is the only part that touches the crystal and therefore provides the only thermal connection to the environment. Thus, the most important requirement for a crystal mount is a good thermalization of the crystal (and light is able to pass it). Of course the mount has to fix the sample but not break it and optimally suits for different crystal shapes as different ROC or even different diameter. For better convenience the crystal can be replaced easily.

Figure 5.1 shows photos of both the old and new crystal mounts. On the left side one can see that the old mount consists of three pieces, the gold plated copper T-piece attached to the cold finger and two clamping pieces out of beryllium copper that hold the sample in place. Four screws each fasten the T-piece to the cold finger and the clamping pieces to each other chucking the crystal which is placed in the through-hole of the T-piece. One can see that the left clamping piece is bent over the convex side of the crystal. There is a thermometer attached to one of the screws to measure the temperature. The thermal contact area between crystal and mount is only the small area where the two beryllium copper clamping pieces press onto the crystal. In addition, the clamping pieces, as they are held together by screws of stainless steel (low thermal conductivity [35]), are not in direct contact with the cold finger like the T-piece and therefore the area with contact to the crystal are not necessarily well thermalized.

In our design of the new crystal mount we continued to use a T-shaped piece attached

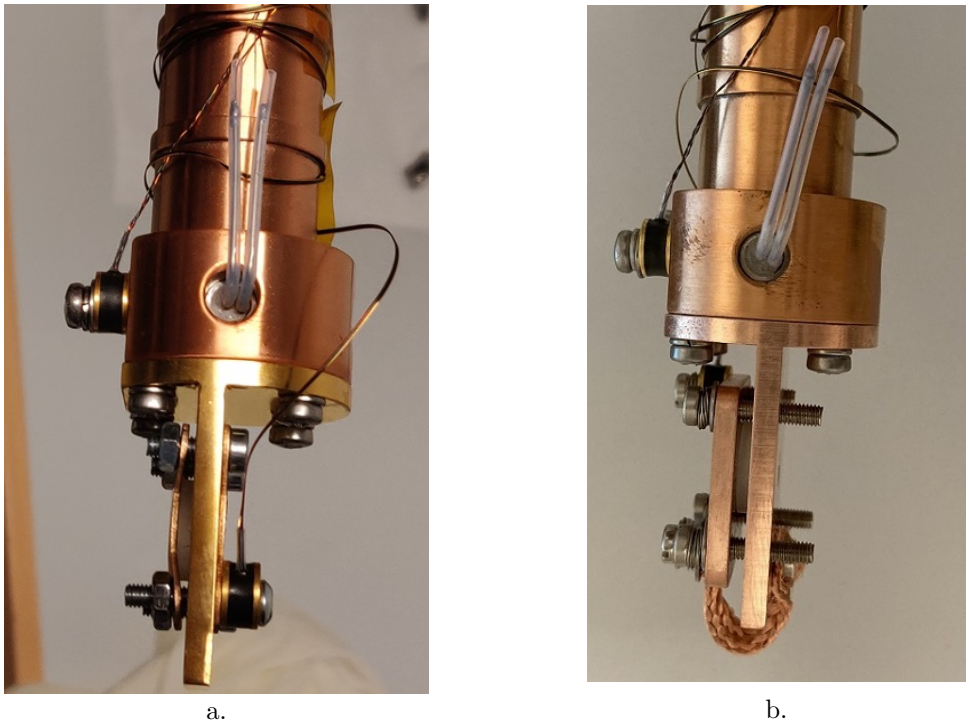

a. b.

Figure 5.1.: Pictures of old (a) and new (b) crystal mounts

to the cold finger. Copper was chosen because it has a high thermal conductivity [35]. In contrast to the old mount the new T-piece has a counterbored through-hole where the flat side of the plano-convex crystal can be inserted to have better thermal contact between the T-piece and the crystal. In this way, the contact area perpendicular to the direction of clamping between the mount and the crystal is increased. The contact of the lateral surface of the crystal with the T-piece is not counted as there is no guaranteed contact. Since the heat transfer rate is proportional to the contact area normal to the clamping force [38], we want as much thermal contact as possible between the mount and the crystal.

For the new crystal mount (construction plans in appendix A) as there is the counterbore the crystal touches directly the T-piece. However increasing the contact area narrows down the through hole. But as the optical and acoustic beam waist are of the order of 100 μm (less than the hole diameter of 5 mm) this should be big enough. In the new construction only one clamping piece with a countersunk through-hole is needed (see figure A.2). The tapered part of the hole prevents a sharp edge from pressing on the convex side of the crystal. The top piece is attached with four stainless screws to the T-piece. Springs between the screw head and the top piece ensure thermal contact with the crystal even with uneven deformation of different materials during cooling and at the same time prevent excessive pressure on the sample. There's a copper braid mounted between both pieces to ensure the thermalization of the top piece. Just like for the old

holder, a thermometer is attached to the least thermalized point for temperature control. For easier handling, the distance between the hole and cold finger was extended a little, so there is more space between the screws and the top piece.

By replacing the crystal mount, the signal was dramatically improved. Looking at the SBS signal with the old crystal mount at 4 K (as shown in fig 5.2a) one can see broad peaks with different shape. Some of them seem to be Lorentzian others have a flat top. The signal between the peaks does not return to the background level as expected. Neighbouring peaks with their broad linewidth do still overlap. The non flat background can be seen well in the full SBS signal sweep.

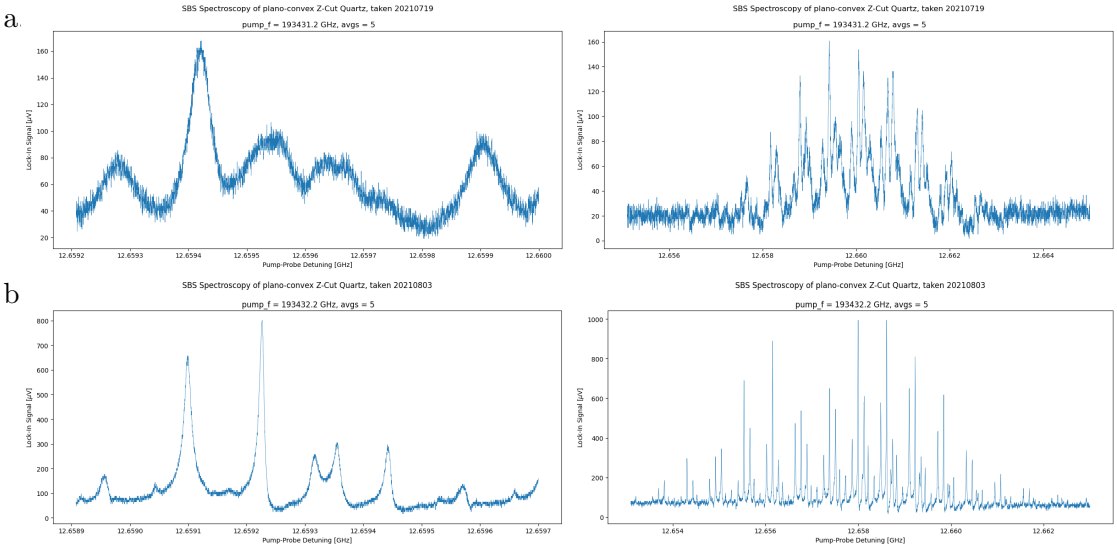

Figure 5.2.: Lock-in signal of plano-convex quartz crystal with old (a) and new crystal mount (b) at $T = 4$ K.

The SBS signals taken with the new crystal mount at 4 K is shown in figure 5.2b. All the peaks are much narrower than with the old mount indicating that the modes are better thermalized. A Lorentzian fit to the highest peak of the left sweep reveals the linewidth to be $\Gamma_m = 4.2$ kHz. In the full SBS signal sweep one can see that the spectrum background is flat. The signal between two peaks reaches the background level. Similar flattening of the background has already been shown by measuring SBS signals of TeO_2 at different cryogenic sample temperatures [34]. We conclude that the thermalization of the crystal is better with the new crystal mount.

The measurements with the two crystal mounts were performed with different laser modes (dither (old) and whisper (new)). In dither mode a strong ~ 1 kHz modulation is applied to the laser in order to stabilize the frequency. However this leads to a forest of sidebands which leads to a laser linewidth is about 50 kHz. The modulation is disabled in the whisper mode which narrows the linewidth to lower than 10 Hz, however the frequency of the laser drifts over time [39]. Therefore we expect a better peak signal resolution from the change of the laser mode. It is quite possible that this had a

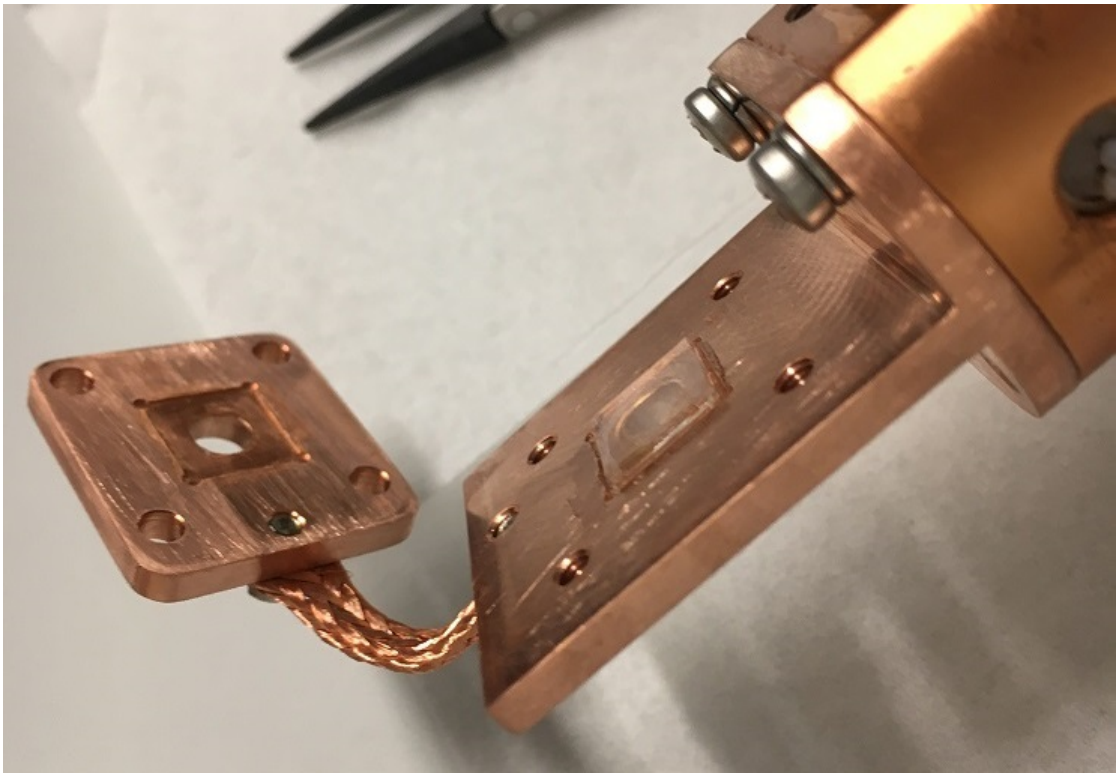

Figure 5.3.: A photo of the open new crystal holder with the CaF_2 crystal inside

significant influence on the measurement differences.

The crystal mount for the two flat-flat crystals (CaF_2 and MgF_2) was constructed similarly to the new mount for the plano-convex quartz crystal. The main differences are the shape and depth of the counterbores as can be see in in figure 5.3. Because of the flat-flat crystals have no curved side the counterbore in the top piece is not tapered anymore. The flat-flat samples have a thickness of only $L = 1$ mm and have a rectangular shape. Therefore both counterbores are only 0.2 mm deep that the counterparts do not touch. Moreover they have a square shape with a side length of 10 mm to ensure that the contact area around the through-hole is still large. Thermalization-wise the mount for flat-flat crystals should show the same properties as the mount for plano-convex crystals.

All the construction plans of the new crystal mounts can be found in appendix A.

5.2. Alignment

As Stimulated Brillouin scattering is a three wave mixing process the measurement setup only works as intended when all three beams are aligned. Thus aligning is a big issue when preparing a measurement. To achieve the maximal optomechanical interaction, all three beams must be collinear and their central axes must match.

The plano-convex crystal is mounted and fixed in the cryostat and hard to move. Therefore it is easier to position light beams in a way that they are aligned to the cylindrical center axis of the crystal. Each beam has several degrees of freedom to set its position and direction in free space. Once setup up as described in section 3, the angle of the collimators, the angle of the mirrors and the x-, y- and z-position of the lenses can be set to align to laser beams.

The biggest challenge is to align the first optical beam to the crystal optimally. It has to be normal to the planar surface of the crystal and cross the crystal along the cylindrical center axis of the dome. This alignment is easier to perform with the pump beam. Because it hits the crystal on its flat surface the reflected signal will only couple back into the pump collimator if the pump is normal to the crystal surface. Monitoring and maximizing the back reflection of the pump beam with a photodiode therefore sets the desired pump direction.

The trickier part is the (x- and y-)positioning of the laser on the crystal. There are two different methods the position it in the center.

Swept back reflection The reflected pump beam is used to align the angle as well as the position of the pump beam incident on the crystal. This is achieved by using the fact that when the pump shines through the crystal on the center axis, the crystal itself is a weak optical cavity. Therefore the reflectivity of the crystal depends on the laser frequency, leading to an oscillation pattern when monitoring the back reflection in time while sweeping the laser frequency. The swept back reflection signal is measured with an oscilloscope (picoscope) that is connected to the output of the photodetector PD1 (Fig. 3.1). Figure 5.4 shows a photo of the oscillation pattern captured when the pump beam is aligned to the crystal. The laser frequency sweep is provided by a tunable diode laser.

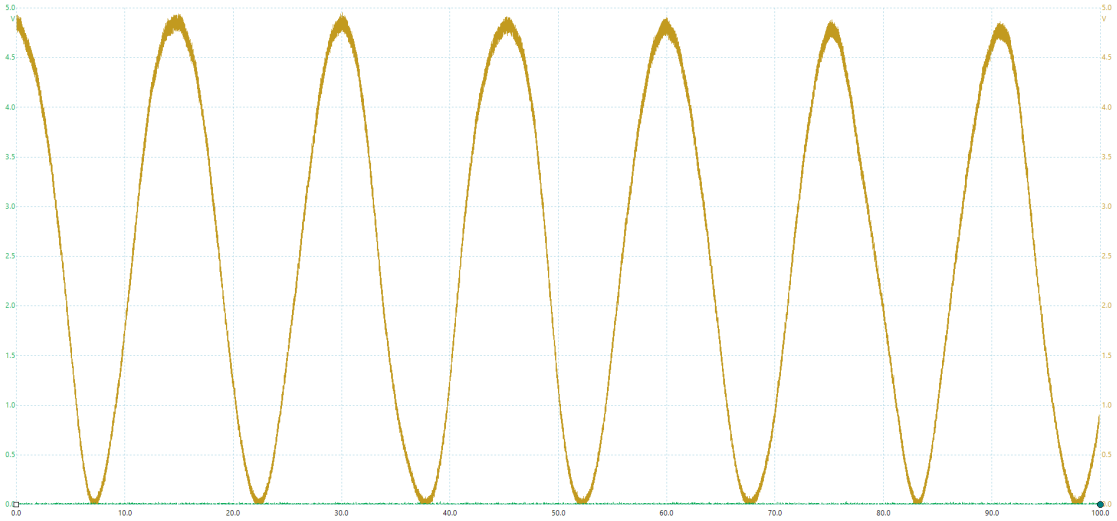

Figure 5.4.: Maximized swept back reflection signal

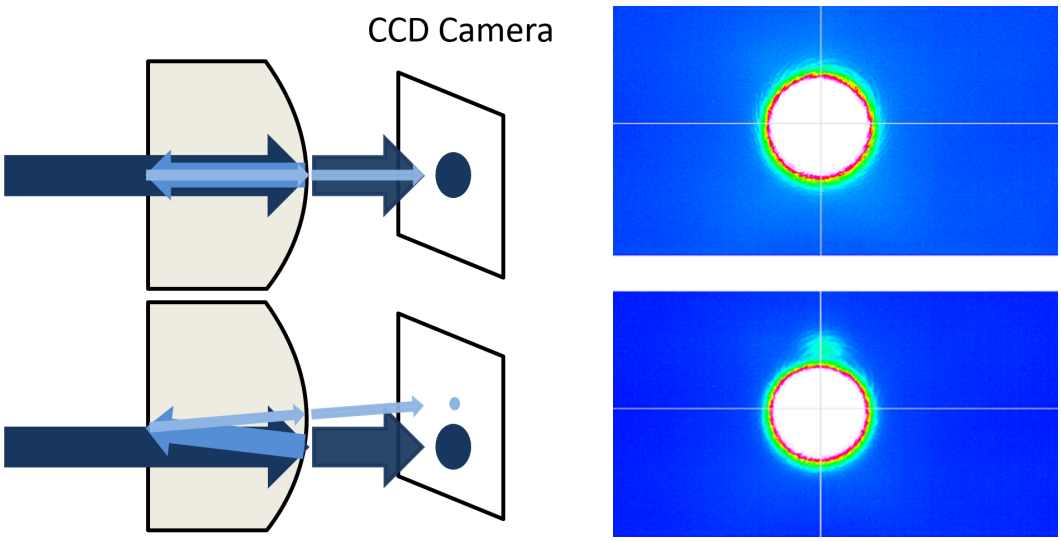

a. Schema of double reflected beam

b. CCD camera pictures

Figure 5.5.: Schemas of double reflected beam (a) and CCD camera pictures (b) of on-axis (top) and off-axis (bottom) pump beam

This method has the advantage that the swept back reflection can be measured without changes in the free space setup. Once the oscillation pattern is found the maximum of the oscillation amplitude is a precise, real-time indicator for having found the center axis of the crystal. The downside of this method is that it only indicates the correct position. The swept back reflection doesn't give a correction indication, if the beam position is far off.

Double reflected beam The laser beam passing the vacuum-crystal boundary has a power reflectance at normal incidence ($R = 4\%$ for quartz) [40]. So every time light crosses the media boundary a small part is reflected. The reflection at the curved surface is crucial for this method. Figure 5.5a demonstrates the basic principle. After being reflected the beam is reflected again at the flat surface and then leaves the crystal in forward direction. Both forward moving beams are detected by a CCD camera after the crystal.

If the pump beam is on the center axis of the plano-convex crystal, the beam is reflected parallel and the double reflected beam has the same position on the CCD camera as the directly transmitted one (top). The picture of the CCD camera is shown in figure 5.5b (top). Since both beams are overlaping only one beam spot is visible. However, if the pump is off-axis, the beam is reflected at a different angle on the curved surface and therefore hits the camera elsewhere (bottom). A weak double reflected beam is visible above the main beam.

The advantage of the double reflected beam method is that for slightly off-center axis

positions as depicted on the bottom of figure 5.5 the signal indicates the direction of the misalignment. Thus when it is difficult to find the swept back reflection, we can use the double reflected beam to find a descent beam position. The disadvantage is that the weak double reflected beam can't be seen when it is at the same position as the transmitted beam, thus in a well aligned position.

Experiments have shown that both methods are expedient. In practice the swept back reflection method has been used more. It is handier as it provides a direct indication of having the intentional alignment set correctly and there's no need to perform multiple measurements to determine the center position. It is convenient to combine both methods within one setup to be able to align faster to the center of the crystal.

Since the two light beams counterpropagate through the crystal, the alignment of the probe laser is much easier. It is sufficient to maximize the coupling of the pump light into the probe collimator with photo detector PD2. This indirectly ensures that probe light overlaps with pump light and therefore is aligned to crystal.

Another upgrade of the alignment is the integration of a more sophisticated translation stage (3-axis NanoMax300, Thorlabs) that enables us to adjust the position of the pump lens with micrometer precision in all 3-axes [41]. The translation stage allows us to reproducibly change the alignment.

The alignment to the center axis of the plano-convex quartz crystal is crucial when it comes to the question of which phonon modes we couple to. Beam propagation code simulations with a off-center forcing functions by 20 μm show that asymmetric modes like the 01 LG mode are driven at comparable amplitudes to the desired fundamental 00 LG mode.

In practice, this can be investigated by changing the pump lens position on the translation stage. Figure 5.6 shows the change of the SBS signal for five different pump lens positions in x direction, where the step length is 10 μm and the signal in the middle (39 μm) is aligned along the center axis of the 10 mm ROC quartz crystal. Because the intensity modulation of this measurement is $\Delta = 487$ kHz the SBS signals of the carrier and the sidebands overlap (see section 3.1 for details). For the aligned signal (39 μm) the peaks (1, 0, 3) are the most dominant ones. All three correspond to the fundamental phonon mode (00 LG). Their peak height decreases as the pump beam is misaligned in both directions. The opposite occurs for the peaks (4, 2, 5). According to the beam propagation simulations the phonon frequency difference between the fundamental and the 10 LG mode is 214 kHz. Their difference in detuning to the fundamental modes in the SBS signal is 216 kHz (216 kHz and 215 kHz, respectively). Thus we refer to them as the 10 LG modes. Their peak height increases with every misalignment step from the center of the crystal. This demonstrates that in the aligned case the light couples more to the fundamental modes whereas in the misaligned situation the light couples strongly to the asymmetric modes as well.

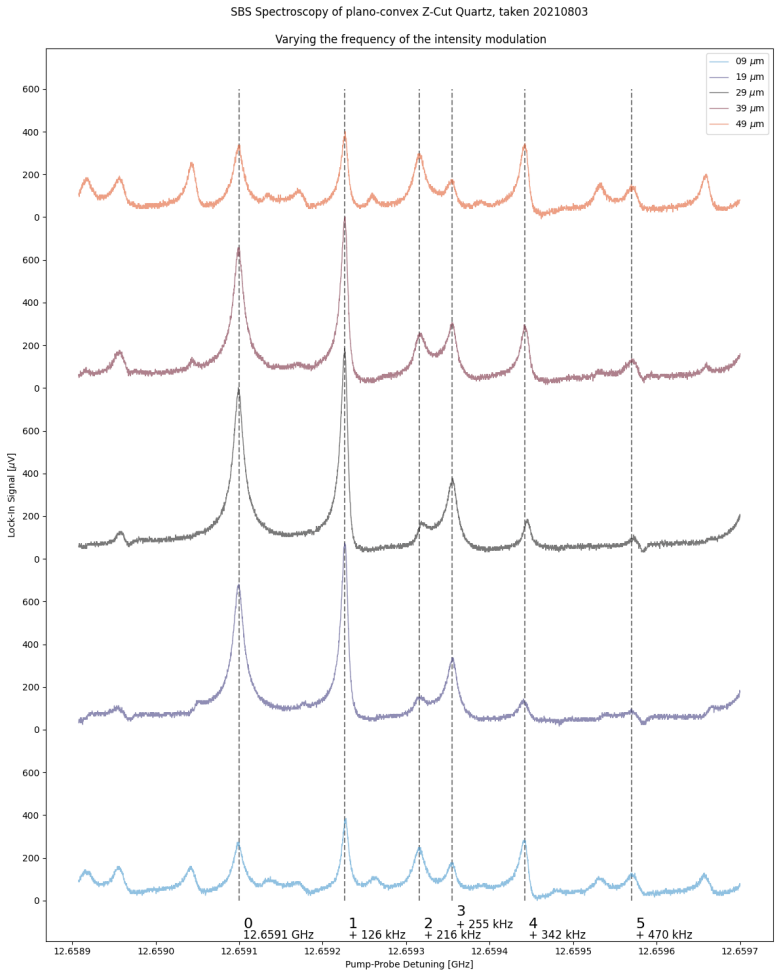

Figure 5.6.: Lock-in signals at different pump lens positions in x-direction on translation stage with plano-convex quartz ($r_c = 10$ mm, $T = 4$ K, $\Delta = 487$ kHz)

5.3. Beam waist

The coupling rate of the optical fields to the phonon modes g_0 and therefore the change of probe power depends on the effective acousto-optical area (see eq. (2.7)). The latter, in turn, depends on the mode overlap of the acoustic and optical fields. In order to get the largest possible signal, we would like to have the largest possible mode overlap of all three beams in the smallest possible area. For being able to do this, we need to know and adjust the beam waists of our beams.

The beam waist w_0 of a Gaussian beam is its width radius w at the focus point, where the width radius is the perpendicular distance between beam axis and the point where the beam intensity has decreased by $1/e^2$ of its peak value [40].

The beam diameter of the acoustic mode is given by the shape and the material of

the crystal and the propagation direction of the phonons. The beam propagation code can be used to simulate the beam diameter of the acoustic mode on the planar surface of the crystal. From this follows that the beam waist of the fundamental acoustic mode of the crystal with ROC $r_c = 30$ mm is $w_a = 45\mu$m on the planar side. When this is fixed the light beams are adjusted consequently.

To achieve the desired overlap the pump beam should be focused onto the flat side of the crystal with a beam waist matching that of the fundamental mode at this position. Therefore the pump beam waist has to match the fundamental acoustic mode ($w_{0,pump} = w_a$).

The probe beam should intersect the pump beam at the curved surface of the crystal. This configuration gives a good uniform effective mode overlap area throughout the crystal what leads to a high Brillouin gain [20]. To determine the beam waist of the probe both laser beams are treated as Gaussian beams. This implies that knowing the beam waist w_0 determines the beam width in every position with distance z away from the focal point via

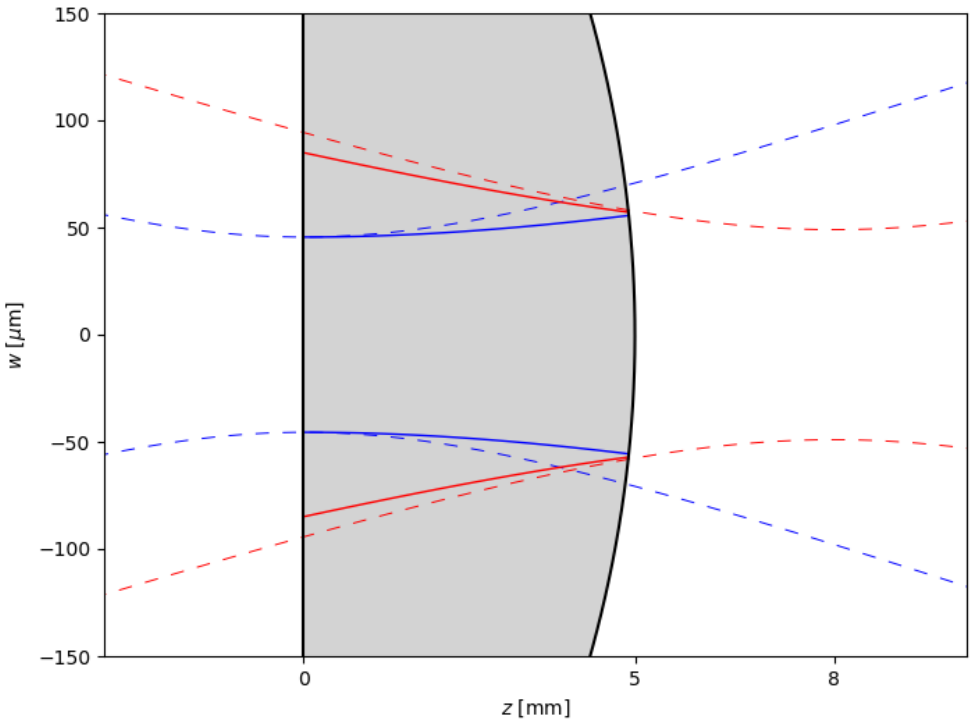

Figure 5.7.: Schema of the optical beams across the plano-convex crystal with crystal length $L = 5$ mm. The pump and probe beam width w in free space (dashed) and media (solid) is shown in blue and red lines, respectively.

$$w(z) = w_0 \sqrt{1 + \left(\frac{z}{n z_0}\right)^2} \tag{5.1}$$

where $z_0 = \frac{w_0^2 \pi}{\lambda}$ with laser wavelength $\lambda = 1550$ nm [40]. Using this Gaussian beam propagation equation (5.1) we find that the desired probe waist is $w_{0,probe} = 49$ μm located 3 mm away from the curved surface. Figure 5.7 shows the desired light beam layout, where the widths of the Gaussian beams in the plano-convex quartz crystal are drawn in solid lines.

As shown in figure 3.2 the free space path of both laser beams start at the collimator. Then the beams are reflected by mirrors and focused onto the desired focus position by means of a lens with focal distances $f = 75$ mm. The resulting beam waist w_0 at the focal point is inverse proportional to the width at the lens [40]. Since at present collimator-

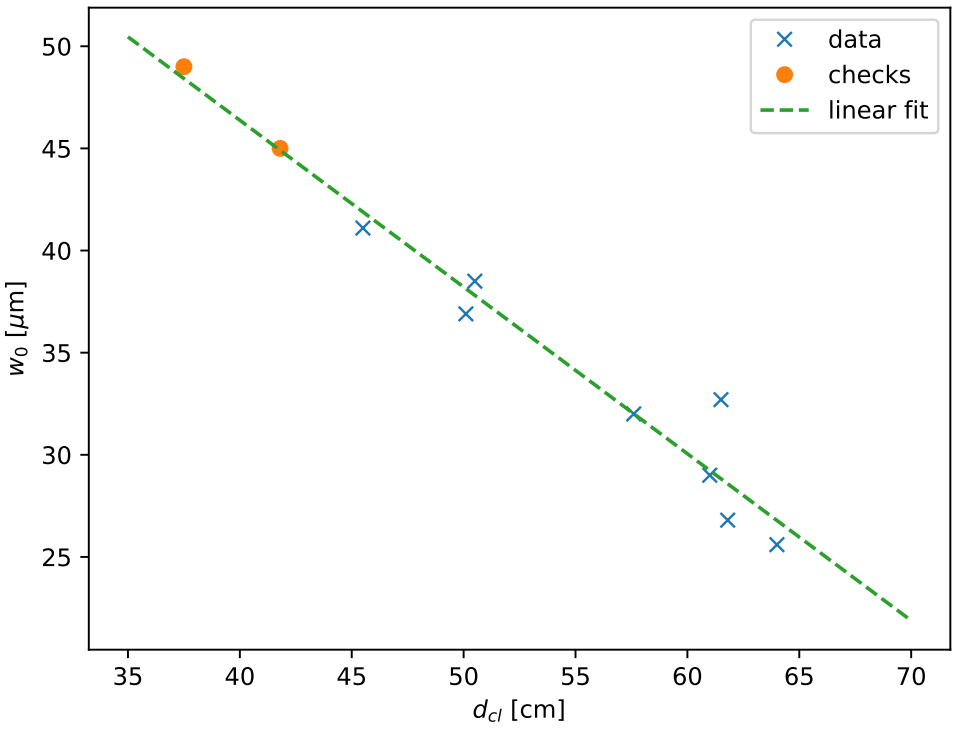

Figure 5.8.: Beam waist w_0 dependent on collimator-lens distance d_{cl}. The dashed line is a linear fit through the measured data, showing the inverse dependency $w_0 \propto d_{cl}^{-1}$. The orange dots show the measured beam waists for the collimator-lens distances used for Brillouin spectroscopy with plano-convex quartz ($r_c =$ 10mm).

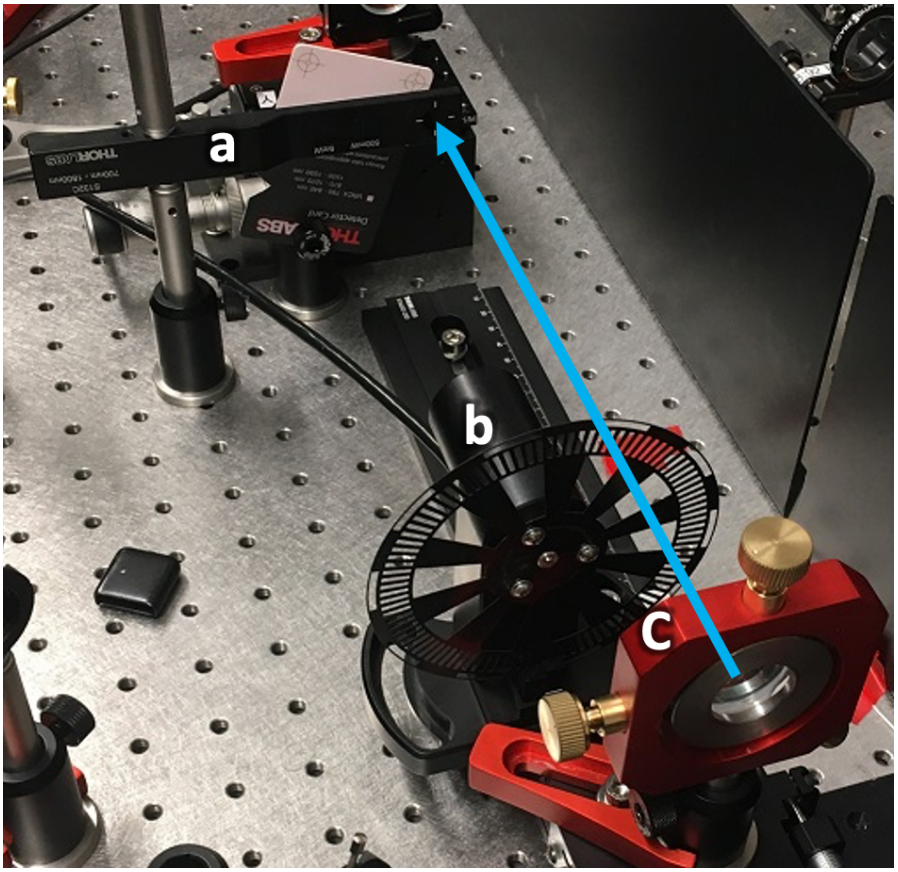

Figure 5.9.: Photo of the beam width measurement setup with the chopper. The blue arrow indicates the beam path. Components: Power meter: (a); Chopper (b); Probe lens: (c).

lens distances d_{cl} the beam width at the lens increases with increasing distance the beam waist at the focal point can be set by choosing the appropriate collimator-lens distance $w_0 \propto d_{cl}^{-1}$.

By measuring the beam waist for different collimator-lens distances the appropriate distances were determined. The measurement results are shown in figure 5.8. The dotted line represents the linear fit through the measured data confirming the $w_0 \propto d_{cl}^{-1}$ relation.

The beam size measurements were performed using a chopper wheel. The measurement setup is depicted in figure 5.9. Thereby the beam width can be determined based on the rise time t_r of the measured beam intensity after the transition of a chopper blade [42]. With the numerical approximated formula [42, 43]

$$2w = 1.56(2\pi f t_r)R \tag{5.2}$$

the beam width of a Gaussian beam can be found. Here f is the frequency of the chopper

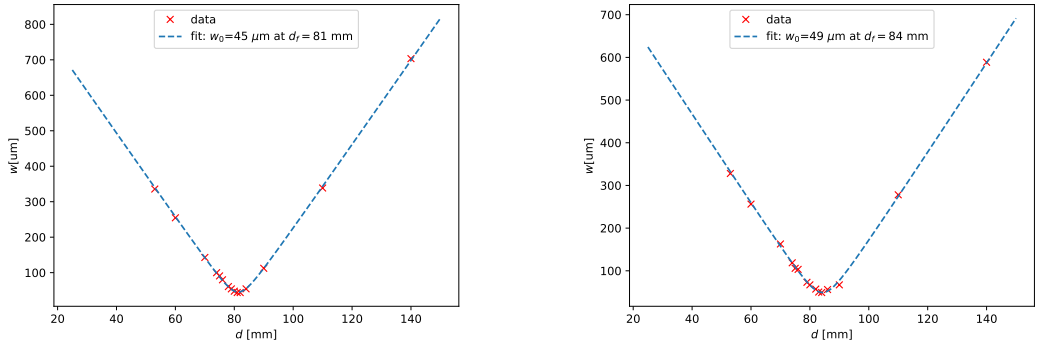

a. $d_{cl} = 418$ mm b. $d_{cl} = 375$ mm

Figure 5.10.: Beam widths w measured at collimator-lens distances $d_{cl} = 418$ mm (a) and $d_{cl} = 375$ mm (b) with chopper method. The dotted line plots the fit assuming Gaussian beam propagation.

and R is the radial position of the laser beam on the chopper wheel. Fitting equation (5.1) through the measured widths at different distances from the lens determines the beam waist.

The beam width measurement results after setting the pump (probe) lens at the found collimator-lens distance $d_{cl,pump} = 418$ mm ($d_{cl,probe} = 375$ mm) to check the intended beam waists are shown in figure 5.10. The measurement points were chosen to be more dense near the focal point. The beam waists obtained from fitting match precisely the desired ones. It is noticeable that the measured distances between the lens and the focal point d_f don't match the indicated focal lengths of 75 mm. One possible explanation is that the reference point of the measurement does not coincide with the center of the lens.

The SBS signals before and after re-adjusting the beam waists are presented in figure 5.11. Both signals are measured with the same 30 mm ROC quartz crystal. Even though the two measurements were performed at different intensity modulation frequencies Δ, they are comparable because both modulation frequencies are higher than the phase-matching bandwidth. The highest peaks of the spectrum before the re-adjustment (see figure 5.11a) has a phonon mode linewidth of $\Gamma_m = 7.5$ kHz. The three peaks within one family match with the beam propagation simulations of the fundamental mode (00 LG) and the two symmetric higher order 10 and 20 LG modes for this crystal. In the SBS signal after the beam waist re-adjustment the peaks match with the simulations of the fundamental (first peak of the family), the symmetric 10 LG (third peak) and antisymmetric 01 LG (second peak). The spectrum shown in 5.11b was measured in the same measurement set as the results from section 4.1. The phonon mode linewidth after the re-adjustment are about 3 times smaller than the ones before.

We conclude that re-adjusting the beam waist did increase the lifetime of the phonon

modes by a factor of 3 as is scales with the reciprocal of the linewidth $\tau_{ph} \propto \Gamma_m^{-1}$. Furthermore the light couples less to the higher order modes, thus there is more coupling with the fundamental mode. Therefore adjusting the beam waist increases the coupling rate to the fundamental mode.

a.

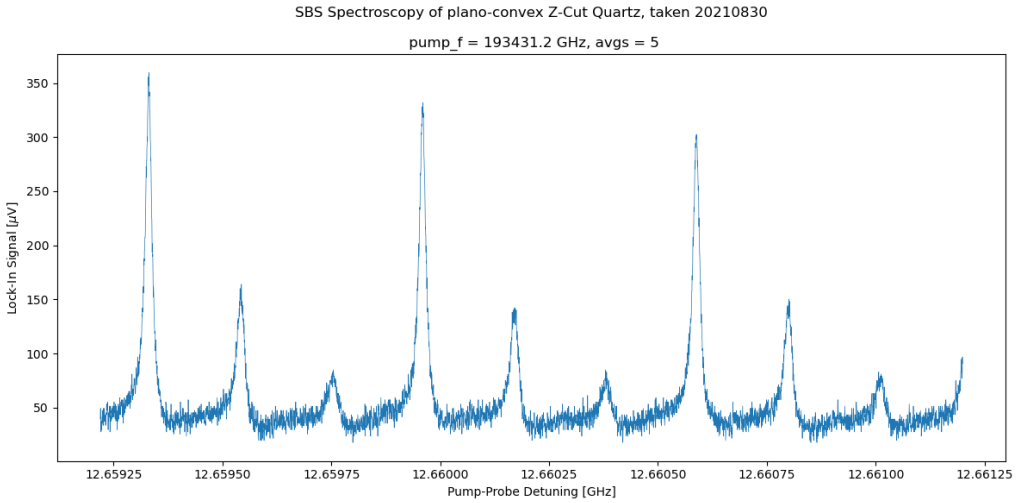

b.

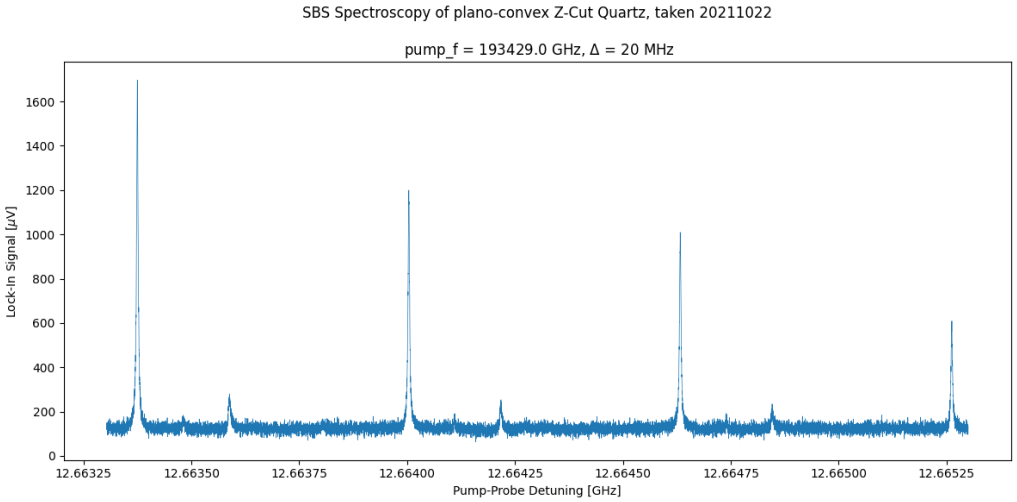

Figure 5.11.: SBS signal before (a) and after (b) adjusting the beam waists with the plano-convex quartz crystal (r_c = 30 mm, Δ = 50 MHz (a) and Δ = 20 MHz (b)) at T = 4 K.

Chapter 6

Conclusion

There were two primary goals of this project. The first was to improve an SBS technique in order to measure long-lived phonon modes. The second was to implement this technique using samples with a variety of materials, shapes and sizes. We successfully managed to achieve both. Our results obtained for a plano-convex quartz crystal at 4 Kelvin show stimulated Brillouin scattering of phonon modes with a linewidth of only $\Gamma = 2.1$ kHz linewidth. This corresponds to a phonon mode lifetime $\tau_{ph} \sim 500\mu$s which is only one order of magnitude lower than the highest phonon mode lifetime measured in such a system [20].

Improvements including designing new crystal mounts for better thermalization of the crystal, development of alignment methods for better acousto-optic mode overlap and adjustment of the laser beam waist to increase optomechanical coupling to the fundamental LG phonon mode have led to a well working Brillouin spectroscopy setup for plano-convex and flat-flat crystals. We were able to characterize two plano-convex quartz crystals with different radii of curvature ($r_c = 10$ mm and $r_c = 30$ mm) and a flat-flat calcium fluoride crystal at cryogenic and room temperature.

We didn't manage to characterize all the materials that we wanted, but we know that this is probably limited by our signal to noise ratio. Using a thicker crystal would improve this. The signal to noise ratio can be further improved by additional filtering of driving frequencies from the scattered signal and implementing a noise cancelling circuit (phase-locked loop) to compensate for crystal vibrations. Furthermore the alignment procedure could be automated, facilitating the measurement process and making it more efficient. Moreover, it would be interesting to further investigate the broad phase-matching bandwidth of the Brillioun signal and the influence of thermalization on the Brillouin spectrum. We suspect that the discrepancies in our measurements of the phase-matching bandwidth with previous measurements [20] is due to angular misalignment of the beams to the phonon mode [34]. Both issues could be approached by performing further measurements and simulations, parts of which we already started.

The Brillouin spectroscopy setup is ready for the characterization of more sample candidates for mediating microwave to optical transduction. This work was an important step in our lab, not only for the results but also for the methods. Now we understand how to align our laser to the phonon modes in a plano-convex crystal which is something we have never done before. That knowledge will have to be transferred to the cavity experiment which will be used for transduction.

Chapter 7

Acknowledgements

I would like to thank Prof. Dr. Yiwen Chu who allowed me to join her research group for this interesting master project, permitting and providing closer insights into hybrid quantum systems. A special thank you goes to Maxwell Drimmer for his supervision, support and guidance through the thesis, he shared his knowledge, his motivation and good mood which were a precious help. Running our snow machine with you has always been a great pleasure. Furthermore I would like to thank the whole Hybrid Quantum Systems group for the likeable atmosphere and the constructive conversations during my thesis. There was always a open door for a quick question or a joke. It was exiting being part of this team and working on future technology. I have really appreciated working with you all. Also I would like to thank my family members for supporting me during all of my studies. Last but not least a big thank you to my girlfriend Anea who gives me great motivation and always puts a smile on my face.

Appendix A

Crystal mount construction plans

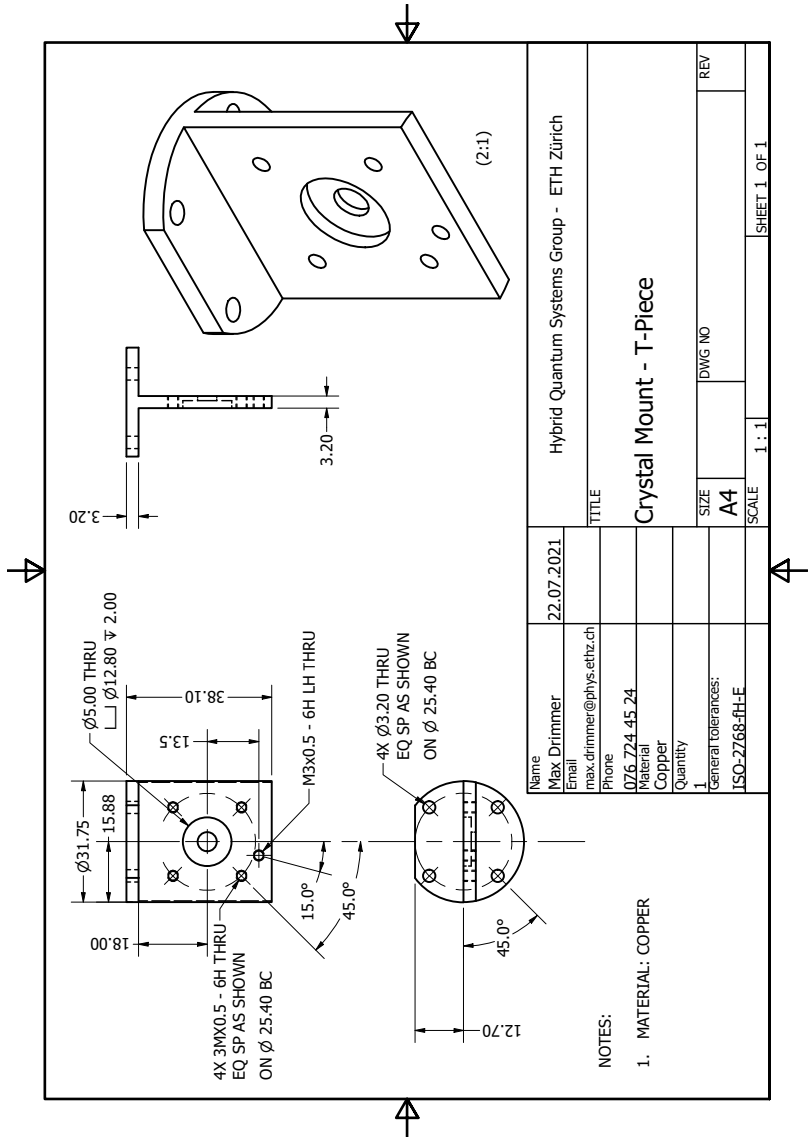

Figure A.1.: Mount for plano-convex crystals - T-piece

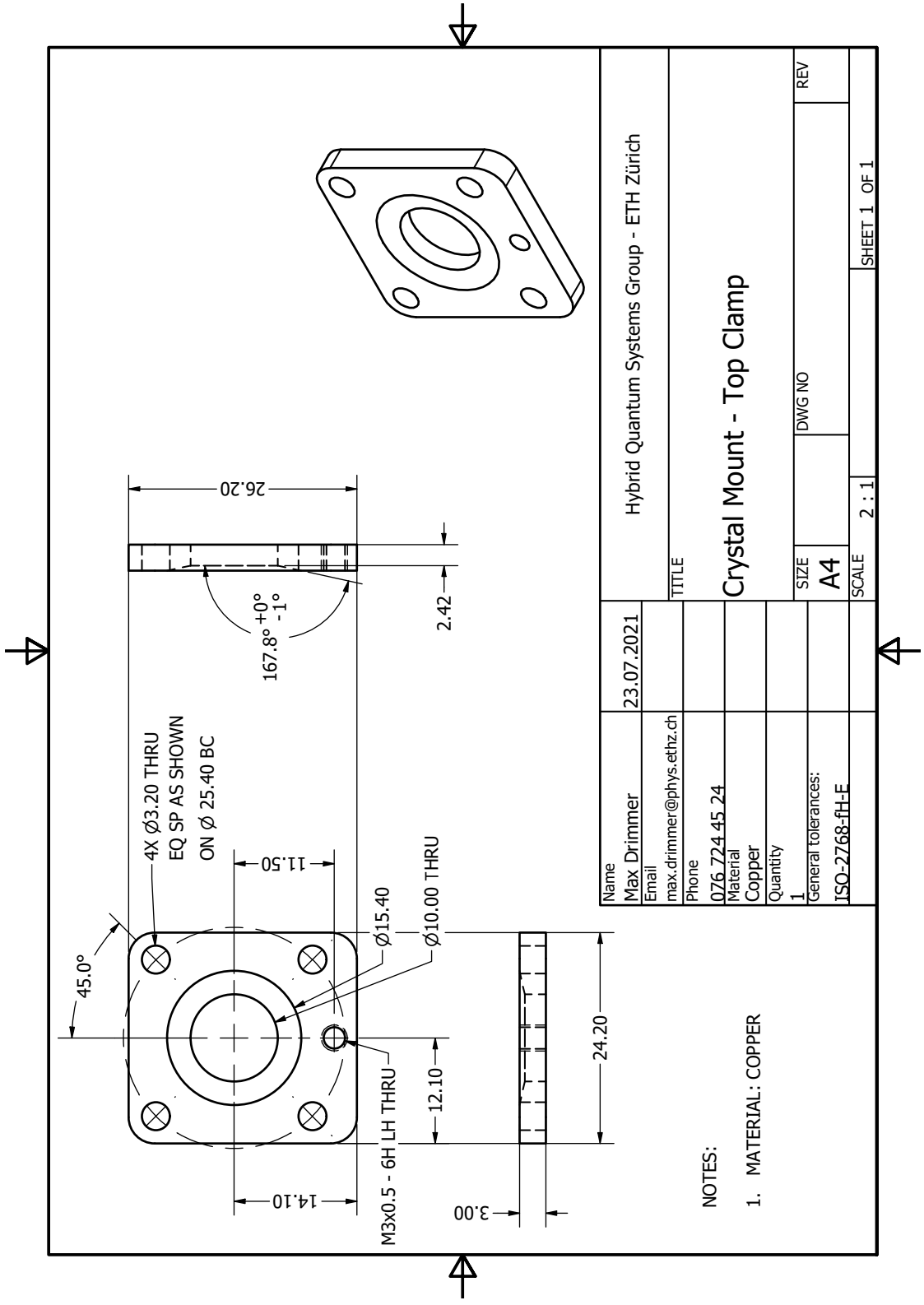

Figure A.2.: Mount for - T-piece crystals - top clamp

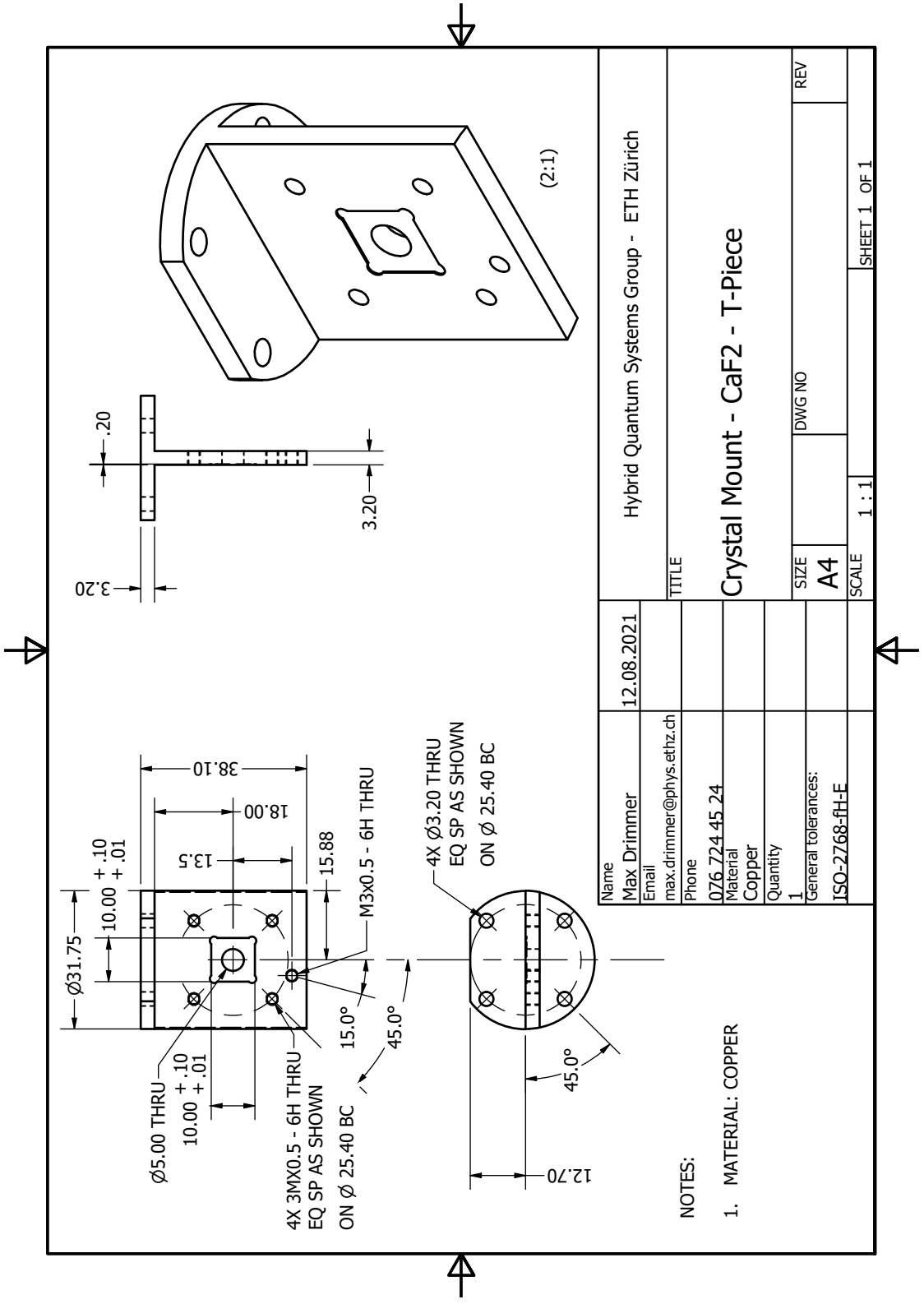

Figure A.3.: Mount for flat-flat crystals - T-piece

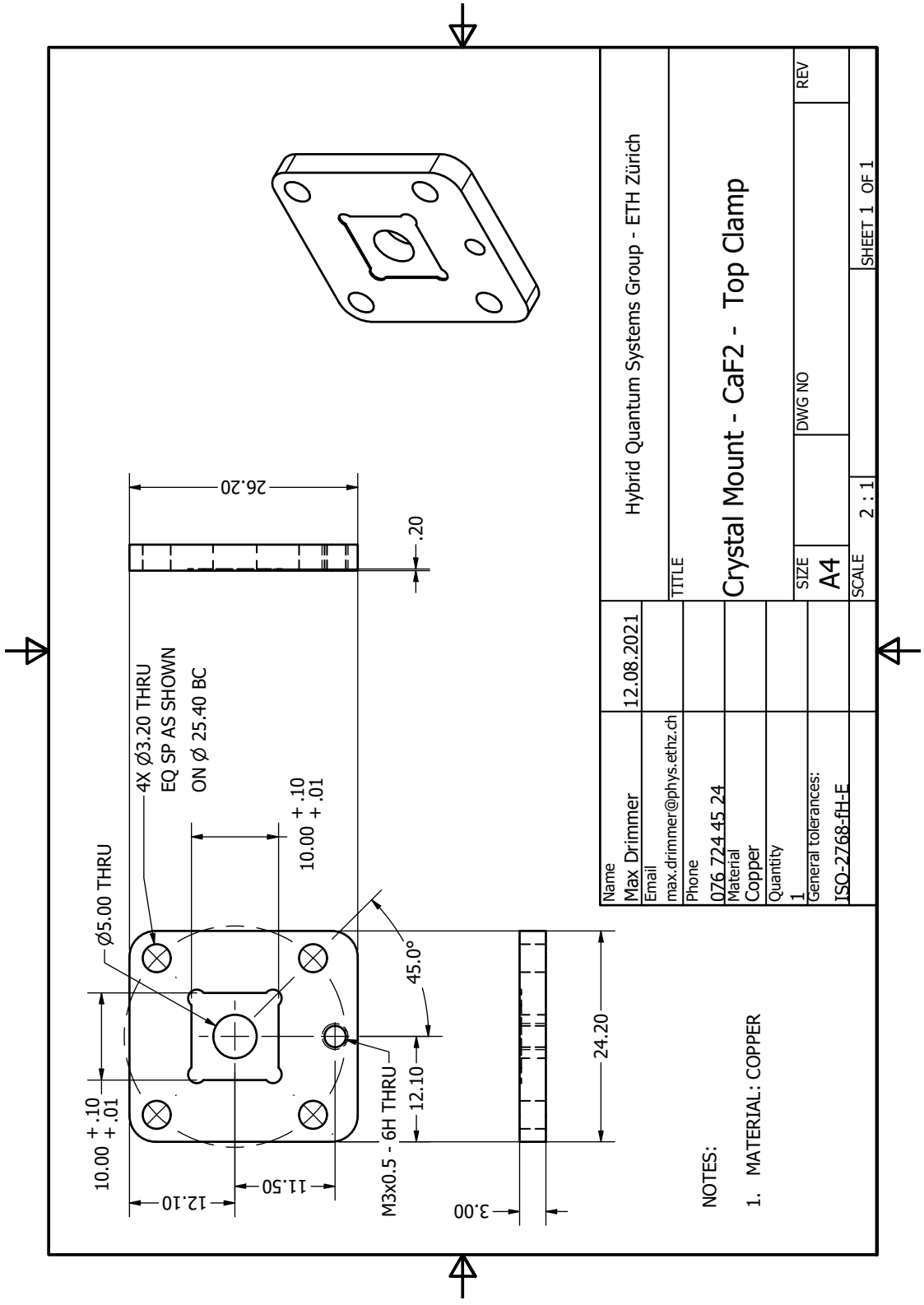

Figure A.4.: Mount for flat-flat crystals - top clamp

Bibliography

1. Arute, F. *et al.* Quantum supremacy using a programmable superconducting processor. *Nature* **574,** 505–510 (2019).
2. Awschalom, D. *et al.* Development of quantum interconnects (quics) for next-generation information technologies. *PRX Quantum* **2,** 017002 (2021).
3. Wehner, S., Elkouss, D. & Hanson, R. Quantum internet: A vision for the road ahead. *Science* **362** (2018).
4. Magnard, P. *et al.* Microwave quantum link between superconducting circuits housed in spatially separated cryogenic systems. *Physical Review Letters* **125,** 260502 (2020).
5. Lambert, N. J., Rueda, A., Sedlmeir, F. & Schwefel, H. G. Coherent conversion between microwave and optical photons—an overview of physical implementations. *Advanced Quantum Technologies* **3,** 1900077 (2020).
6. Riedinger, R. *et al.* Remote quantum entanglement between two micromechanical oscillators. *Nature* **556,** 473–477 (2018).
7. Wang, C. *et al.* Integrated lithium niobate electro-optic modulators operating at CMOS-compatible voltages. *Nature* **562,** 101–104 (2018).
8. Fu, W. *et al.* Cavity electro-optic circuit for microwave-to-optical conversion in the quantum ground state. *Physical Review A* **103,** 053504 (2021).
9. Chu, Y. *et al.* Creation and control of multi-phonon Fock states in a bulk acoustic-wave resonator. *Nature* **563,** 666–670 (2018).
10. Shandilya, P. K., Lake, D. P., Mitchell, M. J., Sukachev, D. D. & Barclay, P. E. Optomechanical interface between telecom photons and spin quantum memory. *arXiv preprint arXiv:2102.04597* (2021).
11. Aspelmeyer, M., Kippenberg, T. J. & Marquardt, F. Cavity optomechanics. *Reviews of Modern Physics* **86,** 1391 (2014).
12. Andrews, R. W. *et al.* Bidirectional and efficient conversion between microwave and optical light. *Nature physics* **10,** 321–326 (2014).
13. Forsch, M. *et al.* Microwave-to-optics conversion using a mechanical oscillator in its quantum ground state. *Nature Physics* **16,** 69–74 (2020).
14. Fiore, V., Dong, C., Kuzyk, M. C. & Wang, H. Optomechanical light storage in a silica microresonator. *Physical Review A* **87,** 023812 (2013).
15. O'Connell, A. D. *et al.* Quantum ground state and single-phonon control of a mechanical resonator. *Nature* **464,** 697–703 (2010).

16. Mason, D., Chen, J., Rossi, M., Tsaturyan, Y. & Schliesser, A. Continuous force and displacement measurement below the standard quantum limit. *Nature Physics* **15,** 745–749 (2019).
17. Kippenberg, T. J. & Vahala, K. J. Cavity optomechanics: back-action at the mesoscale. *science* **321,** 1172–1176 (2008).
18. Chan, J. *et al.* Laser cooling of a nanomechanical oscillator into its quantum ground state. *Nature* **478,** 89–92 (2011).
19. Higginbotham, A. P. *et al.* Harnessing electro-optic correlations in an efficient mechanical converter. *Nature Physics* **14,** 1038–1042 (2018).
20. Renninger, W., Kharel, P., Behunin, R. & Rakich, P. Bulk crystalline optomechanics. *Nature Physics* **14,** 601–607 (2018).
21. Schatteburg, T. *Microwave-to-optical transduction using high-overtone bulk acoustic wave resonators* PhD proposal (ETH Zürich, 2021).
22. Chiao, R., Townes, C. & Stoicheff, B. Stimulated Brillouin scattering and coherent generation of intense hypersonic waves. *Physical Review Letters* **12,** 592 (1964).
23. Boyd, R. W. *Nonlinear optics* (Academic press, 2020).
24. Kharel, P. *et al.* Ultra-high-Q phononic resonators on-chip at cryogenic temperatures. *Apl Photonics* **3,** 066101 (2018).
25. Kharel, P. *et al.* High-frequency cavity optomechanics using bulk acoustic phonons. *Science advances* **5,** eaav0582 (2019).
26. Kharel, P. *et al.* Multimode strong coupling in cavity optomechanics. *arXiv preprint arXiv:1812.06202* (2018).
27. *HF2 User Manual* (Zurich Instruments AG, 2020).
28. *TEST REPORT - Ultra-Narrow Band-Pass Filter Module* IXC-FBG-PS-M-1550-4. iXblue Photonics (Dec. 2020).
29. *Athermal FBG - TEST REPORT* IXC-FBG-PS-1550-3-ATH. iXblue Photonics (Dec. 2020).
30. Thorlabs. *PDB4x5 Series Operation Manual* (visited on 2021-12-13). `https://www.thorlabs.com/thorproduct.cfm?partnumber=PDB415C` (2021).
31. RP Photonics Consulting GmbH. *Balanced photodetection* (visited on 2021-12-13). `rp-photonics.com/balanced_photodetection.html` (2021).
32. Wikimedia commons - Kes01. *Laguerre-Gaussian modes* (visited on 2022-01-12). `https://commons.wikimedia.org/wiki/File:Laguerre-Gaussian_modes.png` (2022).
33. Bernasconi, A. C. *Designing Acoustic ModeShapes for Microwave to Optical Transduction* MA thesis (ETH Zürich, 2021).
34. Ohno, S., Sonehara, T., Tatsu, E., Koreeda, A. & Saikan, S. Spectral shape of stimulated Brillouin scattering in crystals. *Physical Review B* **92,** 214105 (2015).

35. Martienssen, W. & Warlimont, H. *Springer handbook of condensed matter and materials data* (Springer Science & Business Media, 2006).

36. Rao, K. V. & Narasimhamurty, T. Photoelastic constants of CaF2 and BaF2. *Journal of Physics and Chemistry of Solids* **31,** 876–878 (1970).

37. Dong, C.-H. *et al.* Brillouin-scattering-induced transparency and non-reciprocal light storage. *Nature communications* **6,** 1–6 (2015).

38. Holman, J. P. *Heat Transfer* (McGraw-Hill, 1997).

39. *Low Noise Tunable Laser* PPCL500. Oure Photonics (Oct. 2017).

40. Saleh, B. E., Teich, M. C. & FUNDAMENTALS, O. *Photonics* (Wiley, 2019).

41. Thorlabs. *MAX300 Series* (visited on 2022-01-04). `https://www.thorlabs.com/thorproduct.cfm?partnumber=MAX313D/M#ad-image-0` (2022).

42. Thorlabs. *Using a Chopper Wheel to Measure Laser Beam Diameter* (visited on 2022-01-04). `https://www.thorlabs.com/newgrouppage9.cfm?objectgroup_id=14181` (2022).

43. Suzaki, Y. & Tachibana, A. Measurement of the μm sized radius of Gaussian laser beam using the scanning knife-edge. *Applied optics* **14,** 2809–2810 (1975).